



## Two-way nesting in split-explicit ocean models: Algorithms, implementation and validation

Laurent Debreu<sup>a,\*</sup>, Patrick Marchesiello<sup>b</sup>, Pierrick Penven<sup>c,d</sup>, Gildas Cambon<sup>b</sup>

<sup>a</sup> INRIA, MOISE Project-Team and Laboratoire Jean Kuntzmann, 51 rue des Mathématiques, 38400 Saint Martin d'Hères, France

<sup>b</sup> LEGOS (UMR 5566: CNES, CNRS, IRD, UPS), Toulouse, France

<sup>c</sup> LPO (UMR 6523: CNRS, IFREMER, IRD, UBO), Plouzané, France

<sup>d</sup> LMI ICEMASA, Department of Oceanography, University of Cape Town, Rondebosch, South Africa

### ARTICLE INFO

#### Article history:

Received 20 September 2011

Received in revised form 7 February 2012

Accepted 13 March 2012

Available online 28 March 2012

#### Keywords:

Two-way nesting

Finite difference method

Modeling

Boundary conditions

Coastal upwelling

### ABSTRACT

A full two-way nesting approach for split-explicit, free surface ocean models is presented. It is novel in three main respects: the treatment of grid refinement at the fast mode (barotropic) level; the use of scale selective update schemes; the conservation of both volume and tracer contents via refluxing. An idealized application to vortex propagation on a  $\beta$  plane shows agreement between nested and high resolution solutions. A realistic application to the California Current System then confirm these results in a complex configuration. The selected algorithm is now part of ROMS\_AGRIF. It is fully consistent with ROMS parallel capabilities on both shared and distributed memory architectures. The nesting implementation authorizes several nesting levels and several grids at any particular level. This operational capability, combined with the inner qualities of our two-way nesting algorithm and generally high-order accuracy of ROMS numerics, allow for realistic simulation of coastal and ocean dynamics at multiple, interacting scales.

© 2012 Elsevier Ltd. All rights reserved.

### 1. Introduction

Despite a tremendous increase in available computing power, the computational cost of numerical ocean models remains challenging, especially as submesoscale dynamics are now being investigated. The use of high spatial and temporal resolutions reduces local truncation errors of discrete numerical schemes and allows for a better representation of small dynamical scales and topographic features. Mesh refinement allows access to higher resolution in areas of interest at a limited computational cost. This paper focuses on improvement to existing mesh refinement methods for structured meshes.

The unstructured grid approach provides a natural solution for mesh refinement owing to its straightforward refinement process, assuming that an efficient meshing tool is available. A new development phase of unstructured grid models has emerged in recent years with several improvements regarding long-standing issues: preservation of geostrophic balance (Maddison et al., 2011); and local/global conservation properties (Hanert et al., 2004; Levin et al., 2006). The reader is referred to Ham et al. (2009), Deleersnijder et al. (2010), and Sidorenko et al. (2011) for an overview of recent achievements. However, the additional numerical cost of unstructured grid modeling and the ratio of computational cost

over accuracy remains to be objectively evaluated and compared to the traditional structured grid approach. In addition, an important challenge for unstructured mesh models is the implementation of local time-stepping algorithms with better numerical properties. To our knowledge, no real progress on this issue has been reported, at least regarding ocean modeling. We expect that our treatment of time refinement in the present study will be profitable to both structured and unstructured grid methods.

Nesting (or embedding) techniques for structured meshes generally consists of a local high resolution grid (HR or child grid) embedded in a coarse resolution grid (CR or parent grid) that provides the boundary conditions. If this is the only transfer of information between the two grids, the model is said to be in *one-way interaction*. If there is also a transfer of information from the child back to the parent grid (update), the model is in *two-way interaction*. The development of two-way methods have been favored by ocean modelers as they present, in principle, a more continuous interfacial behavior. The various two-way interaction schemes mainly differ by the type of interpolation, location of dynamical interface (the grid points where update is set to occur), conservation properties and type of update (full update or weaker interaction). A recent review of two-way embedding algorithms can be found in Debreu and Blayo (2008), along with recent applications focusing on upscaling impact (Biaostoch et al., 2008); fine-scale dynamics (Marchesiello et al., 2011); and topographic refinement (Sannino et al., 2009). The definition of grid refinement in the

\* Corresponding author. Tel.: +33 4 76 51 48 60; fax: +33 4 76 63 12 63.

E-mail address: [Laurent.Debreu@imag.fr](mailto:Laurent.Debreu@imag.fr) (L. Debreu).

embedding approach generally requires coarse and fine grids to fully overlap. In case of complex geometry (i.e., with rivers and estuaries), this can be a drawback since the coarse grid domain may have to be unnecessarily large. In this case, a more powerful alternative is the composite grid formulation where grids only overlap in connecting areas (Warner et al., 2010). This formulation is not explicitly addressed here but our treatment of mesh refinement is relevant to both embedded and composite grid methods.

In this paper, we present and evaluate a set of choices made in an implementation of two-way nesting methods allowing simultaneous spatial and temporal refinement in a split-explicit, free surface ocean model. In split-explicit time-stepping, fast barotropic quantities are integrated forward in time at a smaller time step than required by the 3D equations. One important question is: how can parent and child grids be coupled at the barotropic level? To our knowledge, this question has not been raised in the literature; reported methods propose that coupling be done at the baroclinic level or that time refinement be avoided altogether (which considerably simplifies the problem). This point is discussed in Section 2.2 after a brief reminder of grid nesting basics (Section 2.1). Section 2.3 focuses on update schemes. In the past, interpolation schemes have received much more attention than update schemes, which often consist of a simple area-weighted average operator chosen for its conservation properties. Here, we propose a scale selective approach to construct the update operator. The respect of conservation properties is another important issue for long term integration. Here, conservation is achieved by flux correction, a classic approach in adaptive mesh refinement for structured grids (Berger and Olinger, 1984; Berger and Colella, 1989). This is presented in Section 2.4 along with its impact on stability and error properties of the resulting scheme. The different methods are evaluated in the idealized case of a baroclinic vortex propagating on a  $\beta$  plane (Section 3). A realistic application to the California Current System is also presented; its results are discussed in light of theoretical arguments and idealized experiments.

## 2. Two-way nesting algorithms

### 2.1. General algorithm

For a general review of two-way nesting algorithms, the reader is referred to Debreu and Blayo (2008). Here, the basic algorithm is briefly described while improvements for various parts of the problem are proposed in the following sections. For simplicity, we consider a single child grid covering a subdomain  $\omega$  of the parent domain  $\Omega$ , as illustrated in Fig. 1. The boundary of the child grid is delimited by the interface  $\Gamma$ .

The coarse resolution grid has a mesh size given by  $\Delta x_H$ , while the fine resolution grid has a mesh size  $\Delta x_h = \Delta x_H / \rho$  where  $\rho$  is the spatial mesh refinement ratio (an integer). The partial differential equations solved by the model are written in the following form:

$$\frac{\partial q}{\partial t} = L(q)$$

along with an initial condition and lateral boundary conditions at the limits of  $\Omega$ . These equations are discretized on the coarse and fine grid domains by:

$$\frac{\partial q_H}{\partial t} = L_H(q_H), \quad \frac{\partial q_h}{\partial t} = L_h(q_h) \quad (1)$$

Thus  $L_H$  and  $L_h$  are discretizations of the same continuous operator  $L$  at different resolutions.<sup>1</sup> The child grid needs lateral boundary con-

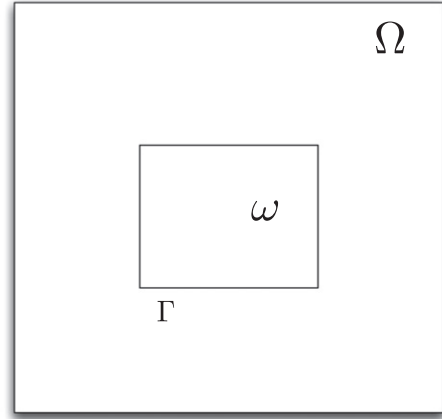


Fig. 1. Local refinement.  $\Omega$  is the domain covered by the coarse resolution grid while  $\omega$  is covered by the high resolution grid.  $\Gamma$  is the boundary of the high resolution domain  $\omega$ .

ditions at the interface  $\Gamma$  and, in two-way mode, the coarse solution is updated using the fine solution. This is modeled by two different operators: an interpolator ( $P$ ) and a restriction operator ( $R$ ). In practice, adequate choices of  $P$  and  $R$  depend on the operator  $L$  and the numerical schemes used for its discretizations  $L_H$  and  $L_h$ . One useful constraint is that these choices do not affect the model solution if the refinement coefficient is 1 (i.e., in this special case:  $L_h = L_H$  and  $q_H$  takes exactly the same values whether nesting is used or not). This constraint ensures consistency of methodology; we thus checked that it is satisfied in all developments presented in the following, i.e., barotropic/baroclinic coupling Section 2.2, conservation Section 2.4, sponge layers Section 2.5.

Assuming that the model is fully explicit, the algorithm can be written in the following simplified form:

1.  $q_H^{n+1} = L_H(q_H^n)$
2. For  $m = 1 \dots \rho_t$  do
 
$$q_h^{n+\frac{m}{\rho_t}} = L_h\left(q_h^{n+\frac{(m-1)}{\rho_t}}\right)$$

$$q_h^{n+\frac{m}{\rho_t}}|_{\Gamma} = P(q_H^n, q_H^{n+1})$$
3.  $q_H^{n+1}|_{\omega} = R(q_h^{n+1})$

Here,  $\rho_t$  is the time refinement factor ( $\rho_t = \frac{\Delta t_H}{\Delta t_h}$ ) and equals the space refinement factor  $\rho$  if the model is restricted to a CFL (Courant Friedrichs Levy) stability condition. Step (1) corresponds to the integration of the coarse grid model for one time step  $\Delta t_H$  on  $\Omega$ , while step (2) corresponds to the integration of the fine grid model for  $\rho_t$  time steps. The interpolator  $P$  makes use of  $q_H^n$  and  $q_H^{n+1}$  to produce space and time interpolations on the interface  $\Gamma$ . In attempting to apply this algorithm to realistic ocean models, several key issues are raised. When the time evolution of state variables is decomposed into two parts (barotropic and baroclinic), the management of grid interaction becomes complex. This is the subject of the next section.

### 2.2. Coupling at the barotropic level

The most restrictive constraint on the time step of a primitive equations ocean model is dictated by the speed of external gravity waves. Several methods could be applied to filter out the fast mode associated with external gravity waves, thus relaxing this constraint. A first choice is to completely remove these waves by applying a rigid lid approximation (Bryan, 1969), leading to the

<sup>1</sup> Note that, in principle, a different choice of numerical schemes and parameterizations may be adopted in the refined grid. However, this would complicate the issue of interface continuity already posed by grid refinement itself.

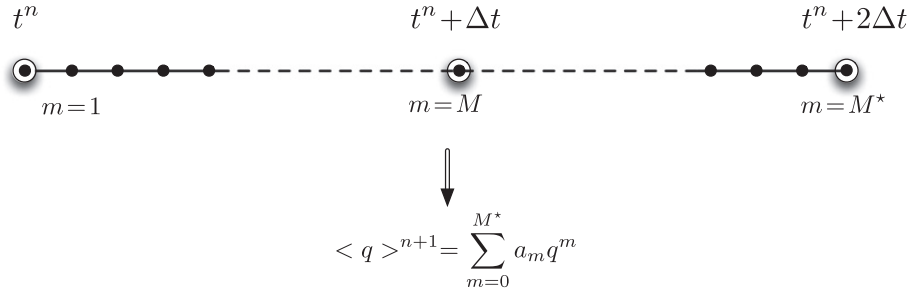


Fig. 2. Time filtering for a uniformly weighted filter ( $a_m = \frac{1}{M^*+1}$ ).

resolution of a barotropic vorticity equation. An alternative approach is an implicit time-stepping method that filters external gravity waves, thereby allowing integration of the free surface equations at the slow mode time step (Dukowicz and Smith, 1994). For such models, the treatment of the fast mode in nested grids has already been tackled in the literature. Laugier et al. (1996) applied local defect correction methods for a rigid lid ocean model, while more recently Haley and Lermusiaux (2010) introduced strongly coupled embedding schemes for free-surface, split-implicit ocean models.

Another widely used method is the split-explicit time integration method of Blumberg and Mellor (1987) and Killworth et al. (1991). In this case, the barotropic time step is a ratio of the baroclinic time step and the barotropic mode is integrated separately. A reported advantage of the split-explicit method is that there is no need to solve a computationally expensive (at high resolution) elliptic system, as opposed to the rigid lid and implicit methods (Killworth et al., 1991). Perhaps more importantly, on numerical grounds, split-explicit methods also provide a better representation of Rossby waves speed than implicit methods that produce large dispersion error. Therefore, new generation oceanic models have generally adopted the split-explicit method, even though it comes with additional complexity at an algorithmic level. Our study proposes solutions to circumvent the difficulties associated with the increased complexity of time splitting in the case of grid nesting.

An important aspect of the split-explicit method is that once the barotropic mode has been integrated, a filtering pass is required in order to remove scales not resolved by the 3D solution (see Shchepetkin and McWilliams, 2005, for a review of these filters), although this may be avoided if the 2D time stepping algorithm is dissipative enough. In order to compute a filtered value of fast quantities (barotropic velocities and free surface) at time  $t_{n+1} = t_n + \Delta t$ , where  $\Delta t$  is the 3D time step increment, the period of integration has to exceed time  $t_{n+1}$ . In the case of grid nesting, this leads to several difficulties that are described in the next paragraph. It should be noted that most existing nesting methods avoid these difficulties by coupling parent and child grids at the baroclinic level only. However, this simpler approach does not provide some of the desired properties of a full coupling between the grids. In particular, it violates the previously mentioned constraint that the model solution be unaffected by nesting in case where the refinement coefficient is one.

### 2.2.1. Problem definition

Let  $M$  be the ratio of the baroclinic and barotropic time steps ( $\Delta t' = \frac{\Delta t}{M}$ ) and  $M^*$  be the number of time steps done in the barotropic mode.  $M^*$  is dependent on the time filter applied for the fast mode. As an example, Fig. 2 presents a uniformly weighted filter over time interval  $[t^n, t^n + 2\Delta t]$  (in this case  $M^* = 2M$ ).

The filtered variables are computed using the following formula:

$$\langle q \rangle^{n+1} = \sum_{m=1}^{M^*} a_m q^m \quad (2)$$

where  $q^m$  denotes an instantaneous barotropic variable (free surface or vertically integrated transport) and where it is required that the weights  $a_m$  be normalized and that the result of (2) be centered at time  $t_n + \Delta t$ , which is equivalent to

$$\sum_{m=0}^{M^*} a_m = 1, \quad \sum_{m=0}^{M^*} a_m m = M$$

Let us now consider the time integration of the embedded model assuming a time refinement factor of 2. Fig. 3 represents the successive steps of time refinement at the baroclinic level while Fig. 4 details the barotropic integration.

From Fig. 4, it appears that the interaction scheme between barotropic quantities at coarse and high resolution can not simply be based on instantaneous values. The coarse grid values are computed at a time ( $t_n + 2\Delta t$ ) greater than their high resolution equivalent ( $t_n + 3\Delta t/2$ ), making it impossible to update the parent from the child grid values. To solve this problem, we propose a method based on interactions between *intermediate* averaged values of fast quantities.

### 2.2.2. Coupling between filtered variables

Let us define the intermediate filtered variables at the barotropic time step  $\alpha$  by the following expression

$$\langle q \rangle_\alpha = \sum_{m=0}^{\alpha} a_{m,\alpha} q^m, \quad 0 \leq \alpha \leq M^* \quad (3)$$

where  $a_{m,\alpha}$  are a new family of weights and where  $\langle q \rangle_\alpha$  is required to be centered at time  $t^n + \frac{\alpha}{M^*} \Delta t \in [t^n, t^n + \Delta t]$ . It is now possible to exchange all required information between parent and child grid solutions through these new variables. During the first child grid time step (step 2 in Fig. 5), the connection between parent

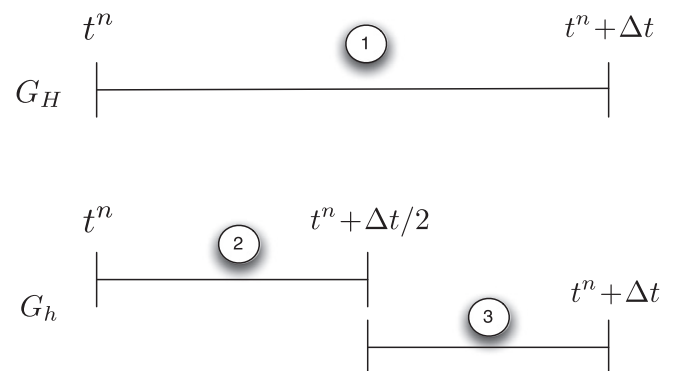
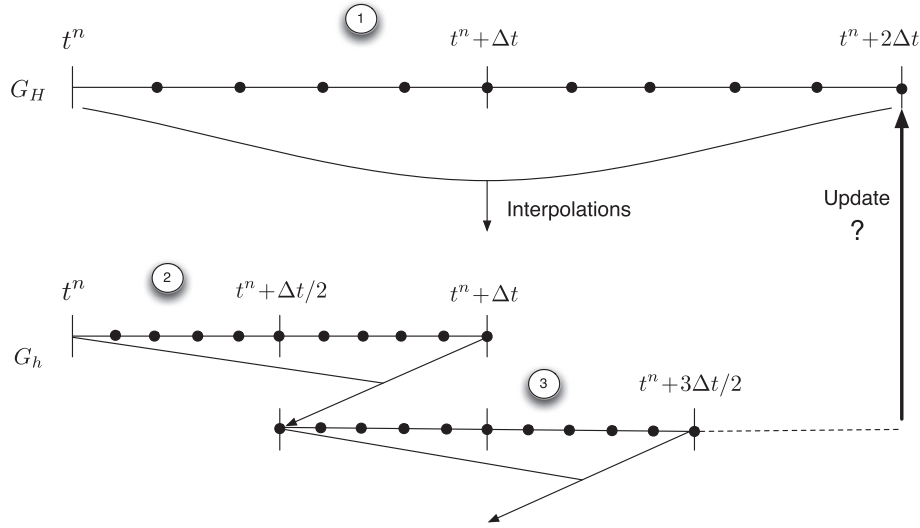


Fig. 3. Time integration at the baroclinic level. Top: parent grid. Bottom: child grid.



**Fig. 4.** Time integration at the barotropic level. The figure represents the position in time of the instantaneous barotropic quantities. The barotropic subcycles are restarted from the previously computed filtered values. Top: parent grid. Bottom: child grid.

and child grid variables,  $q_H$  and  $q_h$ , is done through the requirement that

$$\langle q_h \rangle_\alpha = \langle q_H \rangle_{\alpha/\rho_t} \iff \sum_{m=0}^{\alpha} a_{m,\alpha} q_h^m = \sum_{m=0}^{\alpha/\rho_t} a_{m,\alpha/\rho_t} q_H^m \quad (4)$$

$\alpha$  is assumed here to be a multiple of  $\rho_t$  but linear interpolation in time is applied when this is not the case. Eq. (4) is consistent since  $\langle q_h \rangle_\alpha$  is centered at time  $t^n + \frac{\alpha}{M^*} \Delta t_h$  while  $\langle q_H \rangle_{\alpha/\rho_t}$  is centered at time  $t^n + \frac{\alpha/\rho_t}{M^*} \Delta t_H = t^n + \frac{\alpha}{M^*} \Delta t_h$ . In step 3 of Fig. 5, this equation is modified to give:

$$\langle q_h \rangle_\alpha = \langle q_H \rangle_{M^*/\rho_t + \alpha/\rho_t} \quad (5)$$

From (4) (or from (5)), we deduce the value of the fine grid variables as a function of the coarse grid variables:

$$q_h^\alpha = \frac{1}{a_{\alpha,\alpha}} \left( \sum_{m=0}^{\alpha/\rho_t} a_{m,\alpha/\rho_t} q_H^m - \sum_{m=0}^{\alpha-1} a_{m,\alpha} q_h^m \right) \quad (6)$$

and a similar (reversed) relation is used in the update step. Additionally, we require that the definition of  $\langle q \rangle_\alpha$  is continuous over the barotropic fine grid steps. Since in step 3, the instantaneous variables are restarted (see Fig. 2) from a previous average value

equal to  $\langle q \rangle^{n+1}$ , we have to enforce  $\langle q \rangle_{M^*} = \langle q \rangle^{n+1}$  which is equivalent to

$$a_{m,M^*} = a_m$$

Given  $a_m, 0 \leq m \leq M^*$ , the weights of the original time filter, we finally obtain that the coefficients  $a_{m,\alpha}$  of the intermediate filters should satisfy the following relations

$$\begin{cases} \sum_{m=0}^{\alpha} a_{m,\alpha} = 1, & \sum_{m=0}^{\alpha} a_{m,\alpha} m = \frac{\alpha}{M^*} M, & \forall 0 \leq \alpha \leq M^* \\ a_{m,M^*} = a_m, & 0 \leq m \leq M^* \end{cases} \quad (7)$$

The way these coefficients are computed in practice is described in the appendix. Fig. 6 shows intermediate weights at barotropic time steps  $M^*/4$ ,  $M^*/2$  and  $M^*$ , for several typical filters. Here  $M$  is taken to be 48 and the different filters are: (a) flat weights over  $[0:2M]$ , (b) flat weights over  $[M/2:3M/2]$ , (c) cosine shape filter and (d) power law shape filter (see Shchepetkin and McWilliams, 2005).

### 2.2.3. Computational advantage

Improvement of the physical solution expected by the treatment of nesting at the barotropic level is paid for by added algorithmic complexity. Nevertheless, it also has a computational

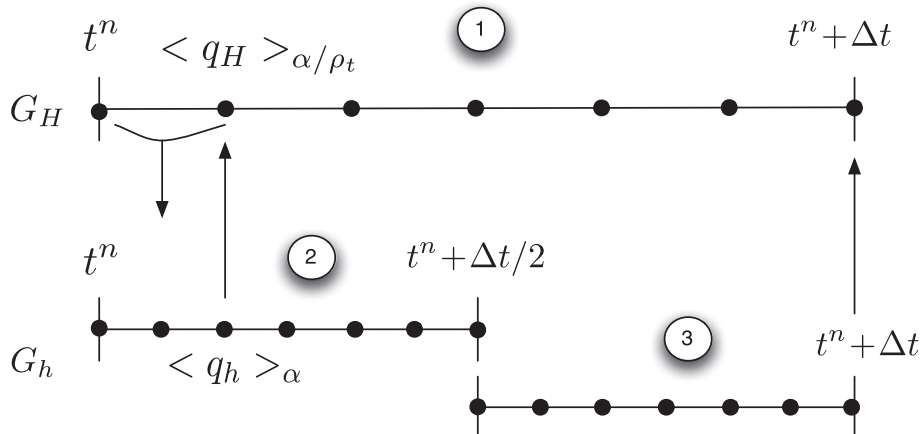


**Fig. 5.** Time integration at the barotropic level. The figure represents the position in time of the intermediate filtered barotropic quantities. Top: parent grid. Bottom: child grid.

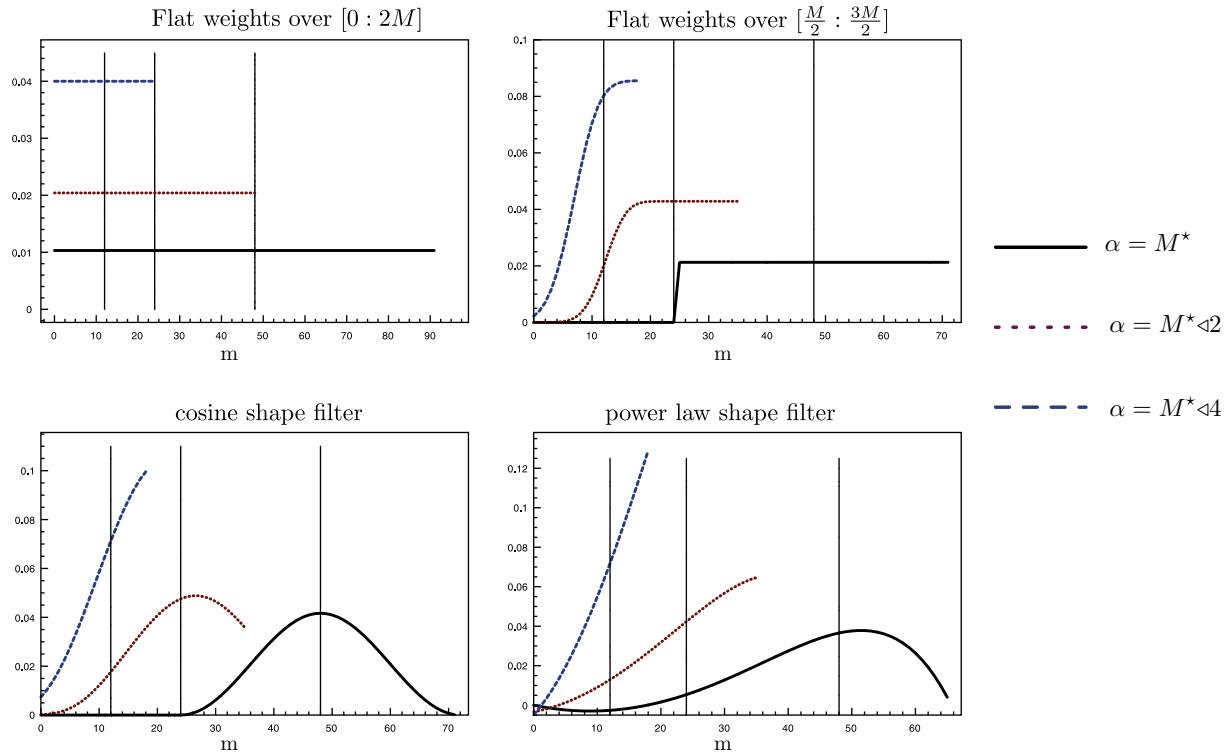


**Fig. 6.** The intermediate weights  $a_{m,\alpha}$  for barotropic time step  $\alpha = M^*/4$ ,  $\alpha = M^*/2$ ,  $\alpha = M^*$  and for different filtering algorithms.  $M = 48$ . The vertical lines indicate the desired average values. Flat weights over  $[0:2M]$  (top left), flat weights over  $[M/2:3M/2]$  (top right), cosine shape filter (bottom left) and power law shape filter (bottom right).

advantage. Nested grids only interact within an interface area whose size is given by the coarse grid operators stencil. The coarse grid solution in the fine grid domain affects neither the fine grid solution nor the coarse grid solution outside the fine grid domain. Therefore, the restriction steps of two-way nesting algorithms need only be applied for coarse grid points located in this interface area. On distributed-memory parallel computers, this significantly reduces the amount of data that needs to be exchanged and the computational gain can be important.

### 2.3. Update schemes

This section is devoted to the study of update (or restriction) operators. For reasons explained in Section 2.4, we do not limit ourselves to what is sometimes referred to as conservative update schemes, i.e. area-weighted averages of the fine grid values. The general design of an update operator should be based on the following two criteria:

- Transfer maximum information to the coarse grid for well-resolved scales on this grid
- Filter scales not resolved on the coarse grid

We study three different update schemes in light of their Fourier symbols: Average; Shapiro Filter; and Full-Weighting. We present these schemes in the one-dimensional case for a mesh refinement ratio of 3; the index  $i$  refers to the index of the child grid point that coincides with the parent grid point:

- Average: The restriction operator is given by

$$\frac{1}{3}(u_{i-1} + u_i + u_{i+1})$$

with Fourier symbol :  $A(\theta) = \frac{1}{3}(1 + 2 \cos \theta)$

where  $\theta = k\Delta x \in [0:\pi]$ ,  $k$  being the wavenumber.

- Shapiro filter: The restriction operator is given by

$$\frac{1}{4}(u_{i-1} + 2u_i + u_{i+1})$$

with Fourier symbol :  $A(\theta) = \frac{1}{2}(1 + \cos \theta)$

- Full-Weighting operator: The restriction operator is given by

$$\frac{1}{9}(u_{i-2} + 2u_{i-1} + 3u_i + 2u_{i+1} + u_{i+2})$$

with Fourier symbol :  $A(\theta) = \frac{1}{9}(3 + 4 \cos \theta + 2 \cos 2\theta)$

The derivation of the full-weighting operator is linked to the definition of so-called first and second orders of a restriction operator as defined by Hemker (2001) in the context of multigrid methods and briefly summarized here:

- A discrete restriction operator with Fourier symbol  $A(\theta)$  is of first order (or low frequency order)  $m$  if  $m$  is the largest integer such that

$$A(\theta) = 1 + O(|\theta|^m), \quad \text{for } |\theta| \rightarrow 0$$

- A discrete restriction operator with Fourier symbol  $A(\theta)$  is of second order (or high frequency order)  $m$  if  $m$  is the largest integer such that

$$A(\theta + 2\pi p/\rho) = O(|\theta|^m), \quad \text{for } |\theta| \rightarrow 0, \quad \forall p \in ]0, \rho[$$

Using these definitions, high order restriction operators can be built for other mesh refinement ratios. It can be shown that the full-weighting operator is second order accurate both at low and high frequencies ( $A(\theta) = 1 + O(|\theta|^2)$  and  $A(\theta + 2\pi/3) = O(|\theta|^2)$ ), that the average operator is of first order 2 and second order 1 and that

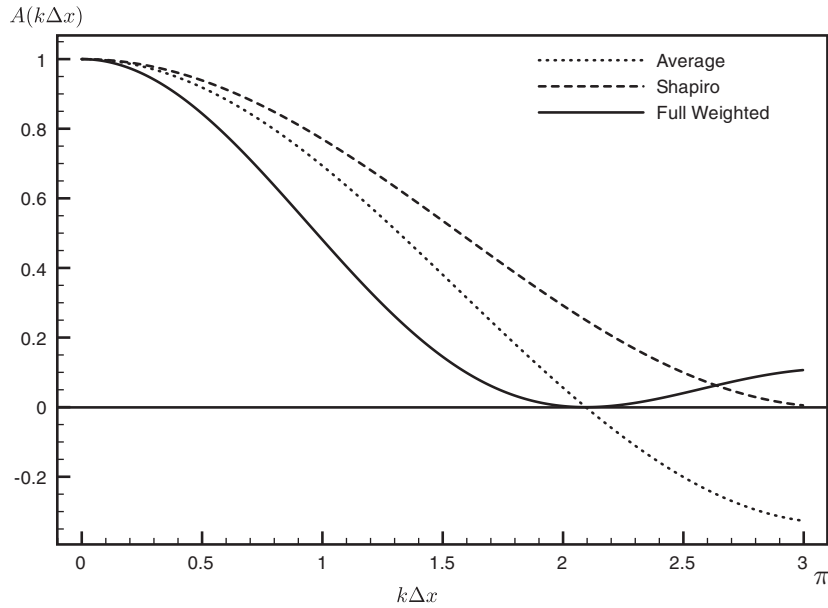


Fig. 7. Amplification factor for typical restriction operators (and for a mesh refinement factor of 3).

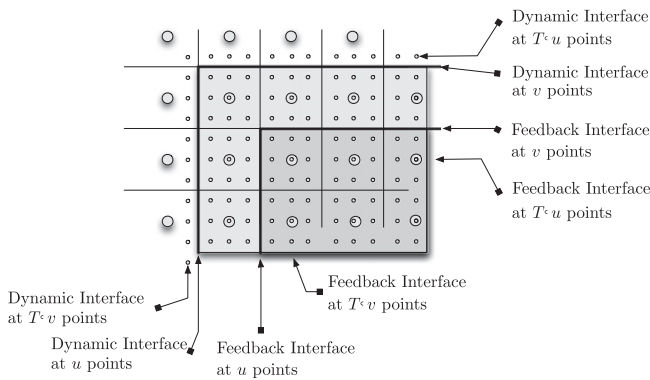


Fig. 8. Separation of dynamic and feedback interfaces on a Arakawa C-grid for a mesh refinement factor of 3. Update occurs in the dark grey area; without interface separation, tracer values and tangential velocities would also be updated in the light grey area.

the Shapiro filter is of first order 2 and second order 0. The symbols are all real, so that there is no dispersion error. The curves of the amplification factors are represented in Fig. 7. What is clearly visible, and will be emphasized by the numerical experiments, is that usual restriction operators apart from the the full-weighting operator are not designed to properly damp subgrid scale features. In practice, this defect has to be corrected by artificially increasing diffusion near the parent/child interface (sponge layers).

### 2.3.1. Separation of dynamic and feedback interfaces

The so-called dynamic and feedback interfaces are sketched in Fig. 8. The dynamic interface denotes the fine grid boundary where the fine solution is forced by the coarse solution; the feedback interface is the outer limit of the area where the coarse solution is updated by the fine solution. There are several reasons for separating dynamic and feedback interfaces (see Debreu and Blayo, 2008) that will be evaluated in the following idealized experiments. One reason comes from the evidence that if noise is produced it will concentrate near the dynamic interface and thus those interface values should not be used to update the parent grid.

### 2.3.2. Free surface, tracer and velocity updates

In a free surface ocean model, for conservation reasons, the discrete time evolution of the free surface elevation can be written in terms of the divergence of a barotropic transport (volumetric fluxes):

$$\eta_{ij}^{n+1} = \eta_{ij}^n - \frac{\Delta t}{\Delta x \Delta y} \left[ U_{i+\frac{1}{2}j} - U_{i-\frac{1}{2}j} + V_{ij+\frac{1}{2}} - V_{ij-\frac{1}{2}} \right] \quad (8)$$

where  $\eta$  is the free surface elevation,  $U$  and  $V$  are barotropic transports in the  $x$  and  $y$  directions and  $i$  and  $j$  are the horizontal grid indices. A consistent update scheme for free surface and barotropic transport can be obtained by applying the restriction operator to the right hand side of this equation. Let's consider the situation represented in Fig. 9 where the mesh refinement factor is equal to 3.

If the free surface restriction operator is a simple average of the nine fine grid cells (and assuming no time refinement), the time evolution of the updated free surface is given by:

$$\begin{aligned} \eta_{i_c j_c}^{n+1} = & \eta_{i_c j_c}^n - \frac{\Delta t}{9 \Delta x_f \Delta y_f} \left[ \left( U_{i_f+\frac{3}{2}j_f-1} + U_{i_f+\frac{3}{2}j_f} + U_{i_f+\frac{3}{2}j_f+1} \right) \right. \\ & - \left( U_{i_f-\frac{3}{2}j_f-1} + U_{i_f-\frac{3}{2}j_f} + U_{i_f-\frac{3}{2}j_f+1} \right) \\ & + \left( V_{i_f-1j_f+\frac{3}{2}} + V_{i_f j_f+\frac{3}{2}} + V_{i_f+1j_f+\frac{3}{2}} \right) \\ & \left. - \left( V_{i_f-1j_f-\frac{3}{2}} + V_{i_f j_f-\frac{3}{2}} + V_{i_f+1j_f-\frac{3}{2}} \right) \right] \end{aligned}$$

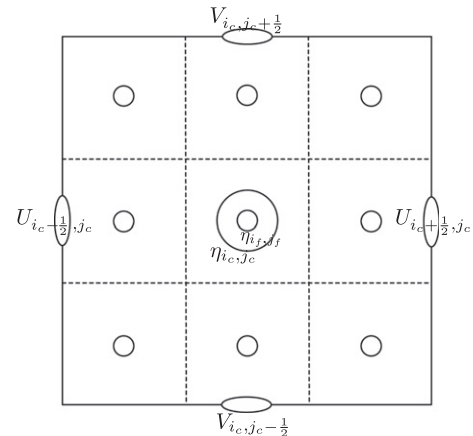


Fig. 9. A coarse grid cell divided in nine fine grid cells on a C-grid.

where  $i_c$  and  $j_c$  are the indices in the coarse grid and  $i_f$  and  $j_f$  in the fine grid (see Fig. 9). In consistence with the average restriction operator for free surface, the coarse grid barotropic transports can be updated by the relations:

$$U_{i_c+\frac{1}{2}j_c} = U_{i_f+\frac{3}{2}j_f-1} + U_{i_f+\frac{3}{2}j_f} + U_{i_f+\frac{3}{2}j_f+1}$$

$$V_{i_cj_c+\frac{1}{2}} = V_{i_f-1j_f+\frac{3}{2}} + V_{i_fj_f+\frac{3}{2}} + V_{i_f+1j_f+\frac{3}{2}}$$

This corresponds for  $U$  to an injection in the  $x$ -direction and an average in the  $y$ -direction and reciprocally for  $V$ . This couple of restriction operators (average for free surface, injection/average for velocities) will be denoted in the following by *update\_mix\_low*. The corresponding high order update schemes will be denoted by *update\_mix\_high* and is the full-weighting operator on free surface, which can be shown to lead for transport variables to a couple of average/full-weighting restriction operators.

For constancy preservation, tracer values should also be updated with the same update operator as the free surface and the three-dimensional velocities (or more precisely volumetric fluxes) should be updated with the same update operator as barotropic velocities. Table 1 summarizes the different restriction operators that will be evaluated.

#### 2.4. Conservation properties by refluxing

On a uniform model grid, conservation is guaranteed when numerical schemes are written in flux form. In two-way nesting procedures, this property is generally lost at the grids interface. Enforced conservation has several computational issues and imposes strong requirements on the intergrid transfer operators that may in turn lead to a loss of accuracy, as will be shown. However, this constraint is recommended for long term integrations. Therefore, after reviewing the basic requirements for conservation on a nested grid, we propose a flux correction algorithm that answers these requirements and present a study of its numerical properties.

##### 2.4.1. Definition and discretization

Let us consider a two dimensional domain and  $q$  the solution of the following equation written in conservative form

$$\frac{\partial q}{\partial t} + \frac{\partial f}{\partial x} + \frac{\partial g}{\partial y} = 0$$

where  $f$  and  $g$  may contain both advective and diffusive fluxes. Then, assuming that the integral of fluxes  $f$  and  $g$  cancels along the boundaries of  $\Omega$ ,  $Q_\Omega$ , integral of  $q$  over the domain  $\Omega$ , is constant in time (at the continuous level):

$$Q_\Omega(t) = \int_\Omega q(x, y, t) dx dy \Rightarrow \frac{dQ_\Omega(t)}{dt} = \int_{\partial\Omega} f ds + \int_{\partial\Omega} g ds = 0$$

In the nested grid system, the quantity  $Q_\Omega$  is defined by the summation over the high resolution domain  $\omega$  and its complement in  $\Omega$ :

$$Q_\Omega = Q_\omega + Q_{\Omega \setminus \omega}$$

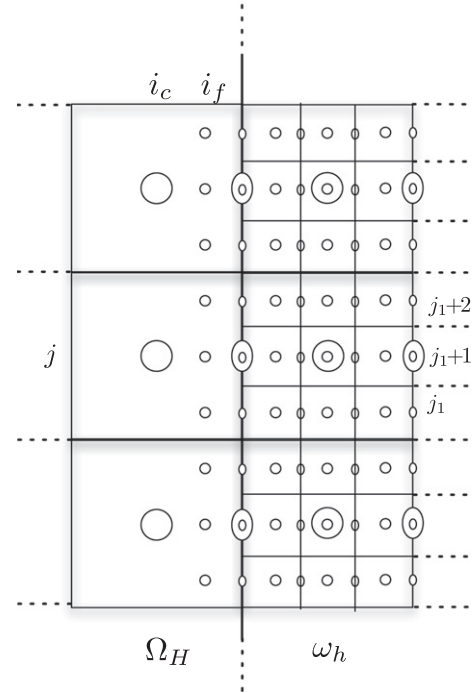


Fig. 10. The coarse resolution domain  $\Omega$  on the left and the high resolution domain  $\omega$  on the right for a C-grid with a mesh refinement factor of 3.

Let us now make the following assumptions for simplicity:

- As illustrated in Fig. 10, we consider a two dimensional domain infinite in both  $x$  and  $y$  directions. The left (resp. right) part of the domain is at coarse (resp. high) resolution. Note that the black thick line in Fig. 10 refers here to the feedback interface which is the relevant interface for conservation issues in two-way nesting.
- The variable  $q_{i_j}^n$  is cell centered
- The time stepping scheme is an explicit Euler scheme

$$q_{i_j}^{n+1} = q_{i_j}^n - \frac{\Delta t}{\Delta x \Delta y} (F_{i+\frac{1}{2}j} - F_{i-\frac{1}{2}j}) - \frac{\Delta t}{\Delta x \Delta y} (G_{i,j+\frac{1}{2}} - G_{i,j-\frac{1}{2}}) \quad (9)$$

where  $F_{i+\frac{1}{2}j}$ ,  $G_{i,j+\frac{1}{2}}$  are volumetric fluxes:  $F_{i+\frac{1}{2}j} = f_{i+\frac{1}{2}j} \Delta y$ ,  $G_{i,j+\frac{1}{2}} = g_{i,j+\frac{1}{2}} \Delta x$ . In a finite volume framework, the definition of  $Q_{\Omega \setminus \omega}$  at discrete level is unambiguously given by

$$Q_{\Omega \setminus \omega}^n = \sum_{i < i_c j} \Delta x_c \Delta y_c q_{i_j}^{c,n}$$

while on the high resolution domain  $\omega$ ,  $Q_\omega^n$  can be defined either using fine grid point values:

$$Q_\omega^{F,n} = \sum_{i \geq i_f j} \Delta x_f \Delta y_f q_{i_j}^{f,n} \quad (10)$$

Table 1

Four choices of restriction operators for free surface ( $\eta$ ), tracers ( $q$ ) and velocities ( $u, v$ ) on an Arakawa C-grid.

Operator	Direction	( $\eta, q$ )	( $u, U$ )	( $v, V$ )
Average	$x$	average	average	average
	$y$	average	average	average
Full-Weighting	$x$	full-weighting	full-weighting	full-weighting
	$y$	full-weighting	full-weighting	full-weighting
<i>update_mix_low</i>	$x$	average	copy	average
	$y$	average	average	copy
<i>update_mix_high</i>	$x$	full-weighting	average	full-weighting
	$y$	full-weighting	full-weighting	average

or using coarse grid point values:

$$Q_{\omega}^{c,n} = \sum_{i>i_c,j} \Delta x_c \Delta y_c q_{ij}^{c,n} \quad (11)$$

In two-way applications, these two expressions are not independent since, inside  $\omega$ ,  $q_{ij}^{c,n}$  is a function of  $(q_{ij}^{f,n})_{ij}$  given by the update operator. Note also that these two expressions are strictly identical only when the restriction operator is a simple area weighted average of the fine grid values.

Let's for the moment assume that the first definition of  $Q_{\omega}^n$ ,  $Q_{\omega}^{f,n}$ , is taken. At discrete level,  $Q_{\Omega}$  at time  $t = t^n$  is then given by

$$Q_{\Omega}^n = \sum_{i \leq i_c, j} \Delta x_c \Delta y_c q_{ij}^{c,n} + \sum_{i \geq i_f, j} \Delta x_f \Delta y_f q_{ij}^{f,n} \quad (12)$$

where, as shown in Fig. 10,  $i_c$  and  $i_f$  denote the nearest coarse and fine grid indices to the left of the interface. Then after one time step, according to Eq. (9) we obtain:

$$\begin{aligned} Q_{\Omega}^{n+1} &= Q_{\Omega}^n - \Delta t_c \sum_j F_{i_c+\frac{1}{2}j}^{c,n} + \Delta t_f \sum_{p=0}^{\rho_t-1} \sum_{j_1}^{j_1+p-1} \sum_{j_f=j_1} F_{i_f+\frac{1}{2}j_f}^{f,n+p/\rho_t} \\ &= Q_{\Omega}^n - \Delta t_c \sum_j \left( F_{i_c+\frac{1}{2}j}^{c,n} - \mathcal{F}_{i_c+\frac{1}{2}j}^{f,n} \right) \end{aligned} \quad (13)$$

where

$$\mathcal{F}_{i_c+\frac{1}{2}j}^{f,n} = \frac{1}{\rho_t} \sum_{p=0}^{\rho_t-1} \sum_{j_f=j_1}^{j_1+p-1} F_{i_f+\frac{1}{2}j_f}^{f,n+p/\rho_t} \quad (14)$$

In general, there will be a misfit between the coarse and fine grid fluxes so that the flux differences on the right hand side do not cancel and conservation is artificially lost:  $Q_{\Omega}^{n+1} \neq Q_{\Omega}^n$ .

If, instead of  $Q_{\omega}^{f,n}$ ,  $Q_{\omega}^n$  is defined by  $Q_{\omega}^{c,n}$  then the discrete integral of  $Q$  is simply given by its summation over the entire coarse grid domain:

$$Q_{\Omega}^n = \sum_{ij} \Delta x_c \Delta y_c q_{ij}^{c,n} \quad (15)$$

In this case, an expression similar to Eq. (13) can be obtained, but this time with a definition of  $\mathcal{F}_{i_c+\frac{1}{2}j}^{f,n}$  that is a function of the restriction operator used for the quantity  $q_{ij}^c$ . If the average restriction operator is chosen, we recover expression (14) which spatially corresponds for the fluxes to the *update\_mix\_low* operator described in paragraph Section 2.3.2 (copy in the  $x$ -direction and average in the  $y$ -direction). If the full-weighting restriction operator is chosen, it can be shown that  $\mathcal{F}_{i_c+\frac{1}{2}j}^{f,n}$  should be computed from the fine grid fluxes using the *update\_mix\_high* restriction operator (average in the  $x$ -direction, full-weighting in the  $y$ -direction).

#### 2.4.2. Flux correction algorithm

In some cases, the flux difference appearing in Eq. (13) can be easily cancelled by applying conservative interpolation. For example, from the time evolution of free surface elevation (Eq. (8)) with no time refinement, it appears that a conservative interpolation of the barotropic transport at the interface must lead to global volume conservation. An example of such second order conservative interpolation for the barotropic transport can be found in Barth et al. (2005). Additional difficulties arise when time refinement is applied and when tracer conservation is desired. To overcome those, we propose a flux correction algorithm inherited from the adaptive mesh refinement community. It follows from the algorithm of Berger and Olinger (1984) and Berger and Colella (1989). The idea is to apply a modification of the coarse grid variables that takes into account the misfit between coarse and fine grid fluxes. Starting from Eq. (13), a correction is applied to the coarse grid variable at time  $n+1$  near the boundary as follows:

$$q_{i_c,j}^{n+1,*} = q_{i_c,j}^{n+1} + \frac{\Delta t_c}{\Delta x_c \Delta y_c} \left( F_{i_c+\frac{1}{2}j}^{c,n} - \mathcal{F}_{i_c+\frac{1}{2}j}^{f,n} \right) \quad (16)$$

This equation implies that the coarse grid variable at index  $j$  has been integrated using, on the right interface, fluxes computed from the fine grid solution:

$$q_{i_c,j}^{n+1,*} = q_{i_c,j}^n - \frac{\Delta t_c}{\Delta x_c \Delta y_c} \left( \mathcal{F}_{i_c+\frac{1}{2}j}^{f,n} - F_{i_c-\frac{1}{2}j}^{c,n} \right) \quad (17)$$

The algorithm is easy to implement assuming that the time evolution of  $q$  can be written in terms of flux divergences, as was indeed the case for the Euler time scheme. The program stores the fine grid fluxes at the boundary and makes a summation in time and space over the fine grid cells. Using this procedure, the overall scheme can be made conservative *whatever the update scheme is*. It implies that the update scheme does not have to be "conservative" (area-weighted average of the fine grid values in a coarse grid cell) and can be constructed entirely with regards to its filtering properties (see Section 2.3).

#### 2.4.3. Choice of $Q_{\omega}$ formulation

As presented in the previous paragraph, the choice of the discrete value of  $Q_{\omega}$  impacts the computation of the equivalent fine grid flux  $\mathcal{F}_{i_c+\frac{1}{2}j}^{f,n}$  and so the flux correction algorithm. The choice between formulations (10) and (11) can be based on the assumption that, as explained in paragraph Section 2.3.2, consistent restriction operators are used for free surface, tracers and velocities (e.g. *average/update\_mix\_low* or *full-weighting/update\_mix\_high*). Then, definition (11) naturally leads to the same restriction operators for the computation of the equivalent fine grid flux. More importantly, the use of the same restriction operators for velocities and fluxes  $\mathcal{F}_{i_c+\frac{1}{2}j}^{f,n}$  is needed to maintain the property of constancy preservation after the flux correction procedure. This formulation will thus be preferred.

#### 2.4.4. Analysis

It is worth analyzing the conservation scheme because, as will be seen, it can be a source of instability. In order to perform a numerical analysis, the problem is reduced to the one dimensional advection equation modified by the flux correction term in Eq. (16). Time refinement is omitted here for simplicity. In this particular case, Eq. (16) can be rewritten

$$q_{i_c}^{n+1,*} = q_{i_c}^{n+1} + \frac{\Delta t_c}{\Delta x_c} \left( F_{i_c+\frac{1}{2}}^n - F_{i_f+\frac{1}{2}}^n \right) \quad \text{since } \mathcal{F}_{i_c+\frac{1}{2}j}^{f,n} = F_{i_f+\frac{1}{2}}^n \quad (18)$$

where we have assumed that an average restriction operator is used for  $q_i^f$  so that both definitions (10) and (11) leads to Eq. (18).

Let us assume that the interpolation at mid-points of the original advection scheme is an approximation of order  $p_1$ :

$$q_{i_f+\frac{1}{2}}^* = g(\dots, q_i, q_{i+1}, \dots) = q_{i+1/2} + \alpha \frac{\partial^{p_1} q}{\partial x^{p_1}} (\Delta x_f)^{p_1} + \text{HOT} \quad (19)$$

HOT stands for High Order Terms. Then the numerical flux is a consistent approximation of the continuous flux at order  $p_1$ , written (assuming a linear flux function  $f$ ):

$$F_{i_f+\frac{1}{2}}^n = f(q_{i_f+\frac{1}{2}}^*) = f(q_{i+1/2}) + f \left( \alpha \frac{\partial^{p_1} q}{\partial x^{p_1}} (\Delta x_f)^{p_1} \right) + \text{HOT}$$

Doing the same for the coarse grid flux leads to

$$F_{i_c+\frac{1}{2}}^n = f(q_{i_f+\frac{1}{2}}) + f \left( \alpha \frac{\partial^{p_1} q}{\partial x^{p_1}} (\Delta x_c)^{p_1} \right) + \text{HOT}$$

Let us further assume that the advection velocity  $u_0$  is constant so that  $f$  is given by  $f(q) = u_0 q$ . Expression (18) becomes:

$$\begin{aligned} q_{i_c}^{n+1,*} - q_{i_c}^{n+1} &= u_0 \frac{\Delta t_c}{\Delta x_c} \left[ \alpha \frac{\partial^{p_1} q}{\partial x^{p_1}} \left( (\Delta x_c)^{p_1} - (\Delta x_f)^{p_1} \right) \right] \\ &= u_0 \Delta t_c \left[ \alpha \frac{\partial^{p_1} q}{\partial x^{p_1}} (\Delta x_c)^{p_1-1} (1 - 1/\rho^{p_1}) \right] \end{aligned} \quad (20)$$

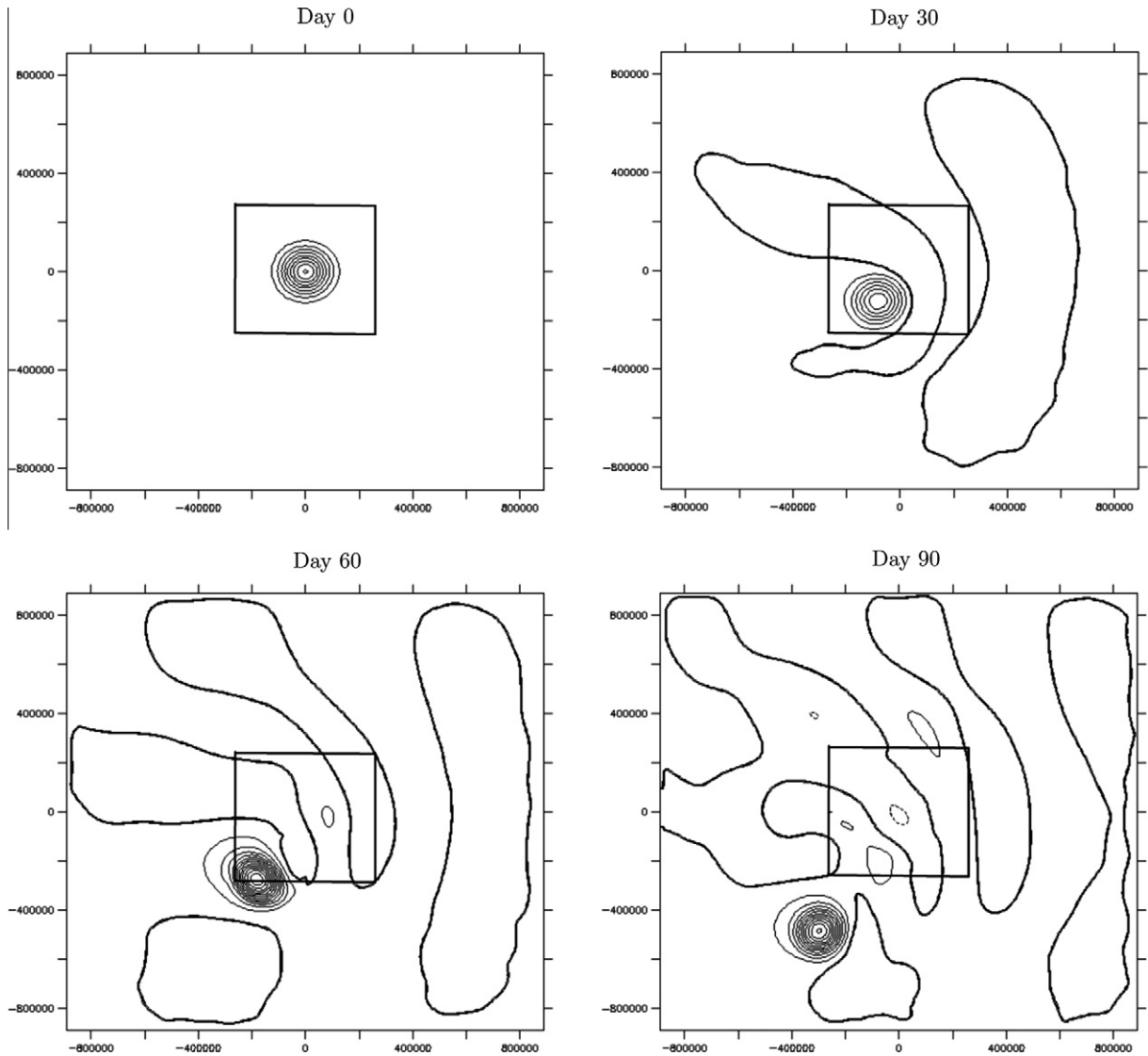


**Fig. 11.** Evolution of surface elevation in the reference, non-nested, high resolution solution. The contour interval is 10 cm. The location of high resolution domain used in nesting experiments is indicated.

It follows from Eq. (20) that the order of approximation near the interface is decreased to  $p_1 - 1$  by the flux correction algorithm. Additionally, if the original advection scheme uses even-order mid-point interpolation, it may affect stability because then (20) may represent anti-diffusion. Moreover, as can be guessed, instabilities are amplified when the mesh refinement ratio  $\rho$  is large.

### 2.5. The sponge layer

Inevitably, small scales produced on the fine grid need to be filtered near the interface to improve continuity between coarse and fine solutions. This is usually done through a so-called sponge layer. In its design, we require that the filter only acts on the scales that are unresolved by the coarse grid. One approach is to damp the difference between coarse and fine grid values near the boundary. In practice, it can be written using a Laplacian diffusion as follows:

$$\frac{\partial q_h}{\partial t} = G_h + \nabla \cdot (\mu \nabla (q_h - q_h^c))$$

where here  $q_h$  denotes any quantities to be filtered (tracers and dynamics) and  $q_h^c$  its equivalent on the coarse grid. To be consistent,

$q_h^c$  must be defined using the restriction operator (used in the update procedure). This can be written as

$$q_h^c = (I_H^h I_h^H) q_h$$

where  $I_H^h$  is an interpolation operator. In two-way nesting,  $I_h^H q_h$  corresponds to  $q_H$  the coarse grid values. The sponge layer is then written as:

$$\frac{\partial q_h}{\partial t} = G_h + \nabla \cdot (\mu \nabla (q_h - I_H^h q_H))$$

where  $\mu$  is a coefficient ranging from its maximal value  $\mu_0$  at the interface to 0 a few grid points away from it (usually at a distance of 3 coarse grid cells). This sponge layer is applied both on momentum and tracers. When applied on tracers, the diffusive fluxes are stored and added to the advective fluxes for later use in the refluxing algorithm Section 2.4.2.

### 3. A ROMS test case: baroclinic vortex

The algorithms presented in this paper were implemented in the Regional Oceanic Modeling System (ROMS; Shchepetkin and

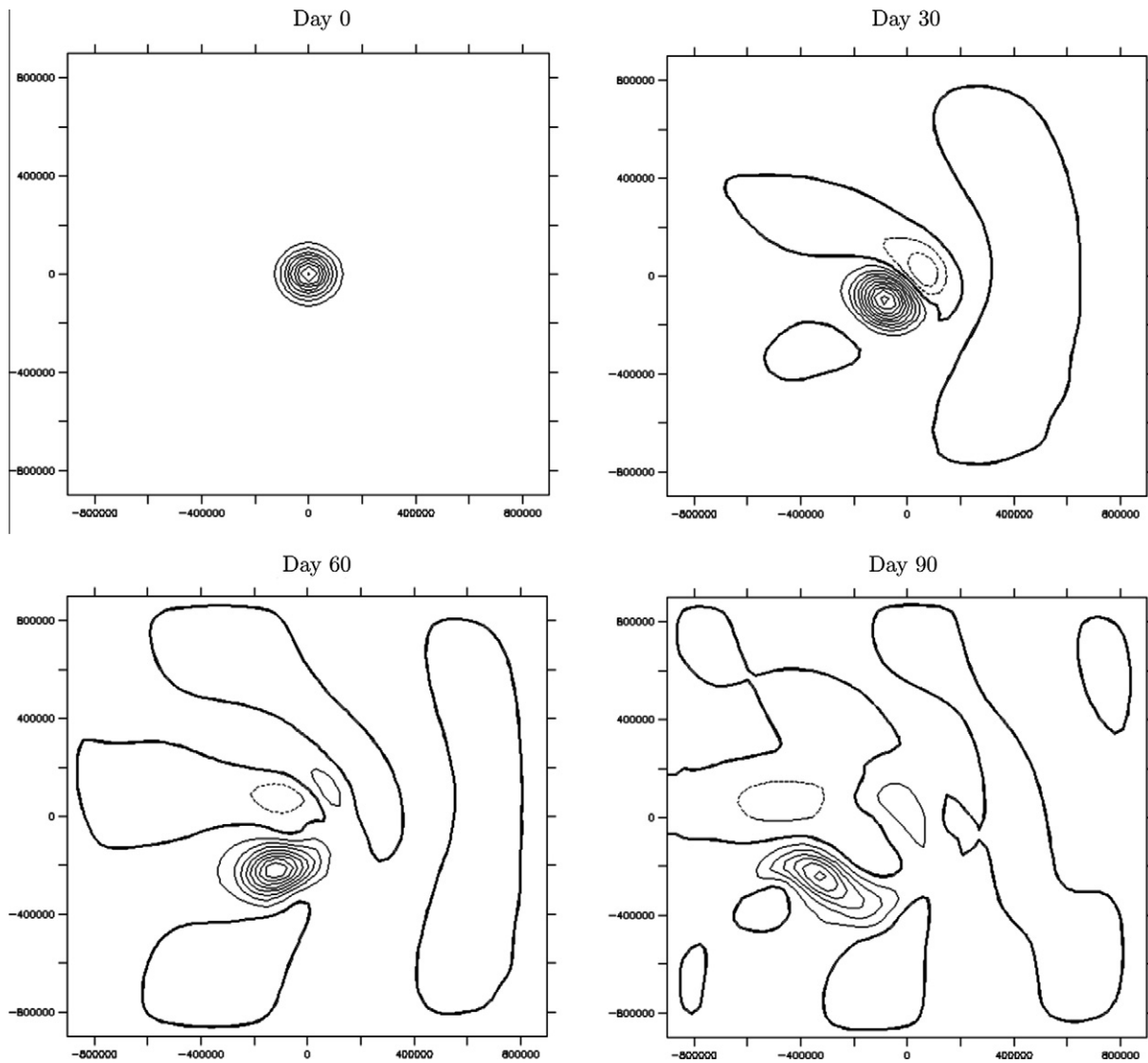


Fig. 12. Evolution of surface elevation in the coarse, non-nested, solution. The contour interval is 10 cm.

McWilliams, 2005) and are here evaluated using the baroclinic vortex test case. The idealized experiment of a baroclinic and initially axisymmetric vortex propagating on a  $\beta$ -plane has been described by McWilliams and Flierl (1979). It has been used to evaluate nesting performances by Spall and Holland (1991) in the case of a rigid-lid model. Its use has been extended by Penven et al. (2006) to free surface models and ROMS one-way nesting. In these applications, as in the present one, performance evaluation is based on the comparison between the nested solution and a reference solution, which is computed on a fine grid over the whole domain.

### 3.1. Model configuration and simulations

A full description of initial conditions and model configuration can be found in Penven et al. (2006) and are only summarized here. The vortex is initialized as a Gaussian surface pressure distribution with a maximum surface geostrophic velocity of  $1 \text{ m}\cdot\text{s}^{-1}$  and a horizontal  $e$ -folding scale of 60 km. We consider a baroclinic vortex in the presence of a continuous background stratification, with no motion below 2500 m. The initial horizontal velocities are in geostrophic equilibrium with the initial pressure field.

The grids are square, on a flat bottom ( $H_0 = 5000 \text{ m}$ ), using a  $\beta$ -plane approximation centered around  $38.5^\circ \text{ N}$ . The parent grid domain is  $1800 \text{ km} \times 1800 \text{ km}$ , while the child grid domain is approximately  $580 \text{ km} \times 580 \text{ km}$ . We use 10 evenly spaced vertical levels, no explicit horizontal viscosity unless specified in sponge areas (there is implicit dissipation in the upstream biased advection scheme), no vertical viscosity, and no bottom friction. The Brünt–Vaissala frequency is fixed at  $N = 0.003 \text{ s}^{-1}$ . The horizontal resolution of the coarse grid is 30 km and the mesh refinement ratio is set to 3, leading to a resolution of 10 km for the child grid. The parent domain is assumed unbounded, which requires open boundary conditions on each side, as described by Marchesiello et al. (2001). The evaluation of the nested solution is made against a reference solution computed with high resolution (10 km) on the whole parent grid domain. In all experiments, we use the power law shape function to compute intermediate filtered variables at the barotropic level since it is already used in ROMS to filter external gravity waves in the barotropic/baroclinic coupling.

The vortex evolution in the reference solution is depicted in Fig. 11 for the free surface elevation. Due to  $\beta$ , the anticyclonic vortex, initially axisymmetric, propagates south-westward and

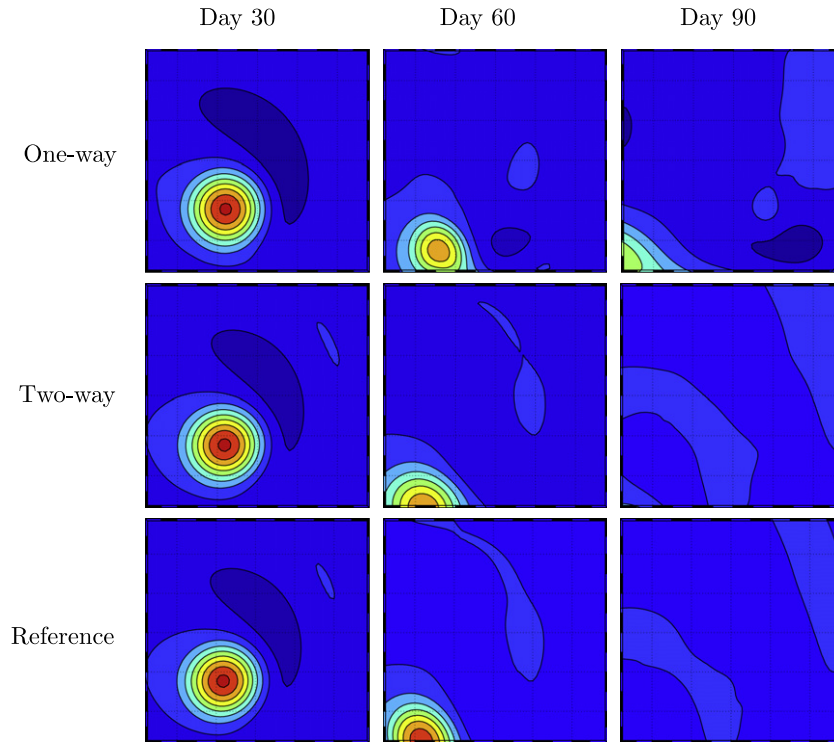


**Fig. 13.** Evolution of surface elevation in the child grid domain for one-way (top), two-way (middle) and reference solutions (bottom). The two-way solution is obtained with *update\_mix\_high* restriction, separate interfaces and sponge layer. The contour interval is 10 cm.

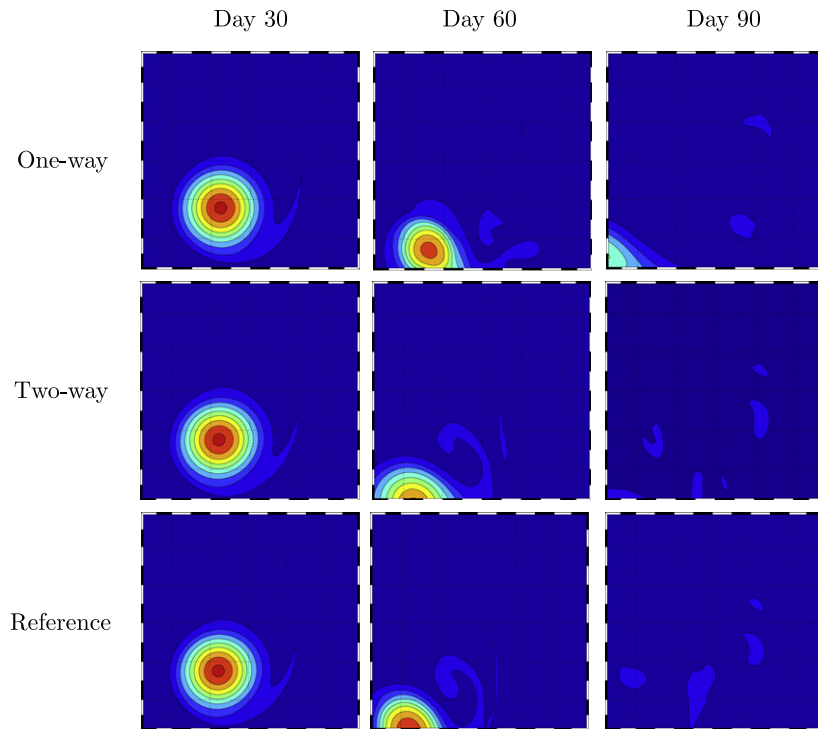


**Fig. 14.** Evolution of temperature [°C] in the child grid domain for one-way (top), two-way (middle) and reference solutions (bottom). The two-way solution is obtained with *update\_mix\_high* restriction, separate interfaces and sponge layer. The contour interval is 0.2 °C.

changes its shape by Rossby-wave dispersion. The vortex retains part of its axisymmetric shape, but weakens as it emits a train of weak-amplitude Rossby-waves mostly in its wake. As explained by McWilliams and Flierl (1979), advective effects compensate

the  $\beta$ -related leakage, preserving the vortex pattern. In the coarse resolution case, the advective axisymmetrisation effects are reduced and the vortex experiences strong dispersion, resulting in loss of integrity (Fig. 12). When grid refinement is applied (Figs.

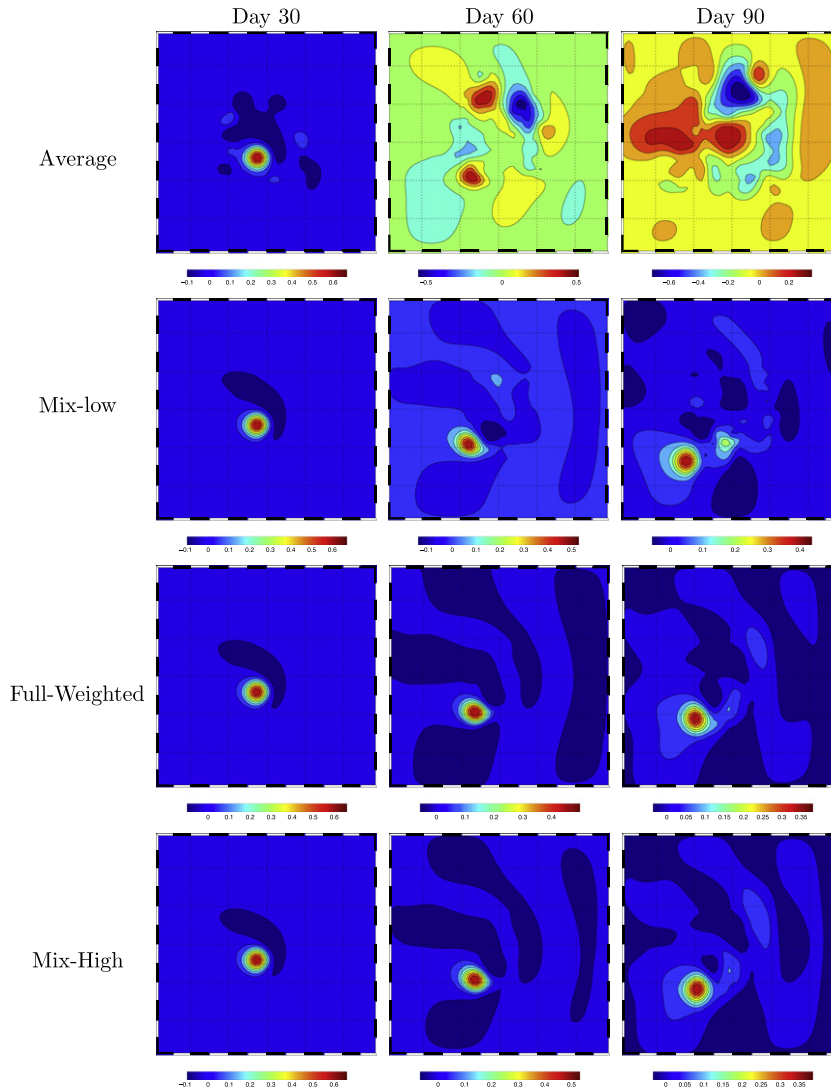


**Fig. 15.** Free surface elevation (on the coarse grid domain) after day 30, 60 and 90 (from left to right) for different update schemes (without sponge layer and without interfaces separation).

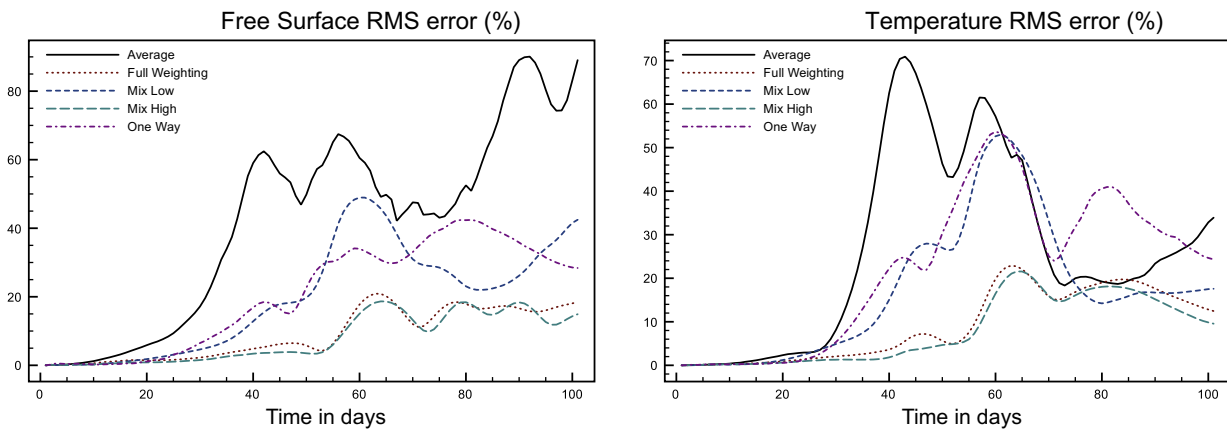


**Fig. 16.** Normalized RMS error [%] in the vortex test case for free surface elevation (left) and temperature (right). In the nesting procedure, neither sponge layer nor interface separation are applied.

13 and 14) in either one-way or two-way mode, most of the high resolution properties are recovered. However, two-way nesting is clearly an improvement over one-way nesting, depending though on the nesting algorithm, as will be shown.

### 3.2. Update schemes

In a first series of experiments, the performance of update schemes presented in Section 2.3 are investigated. All the simula-

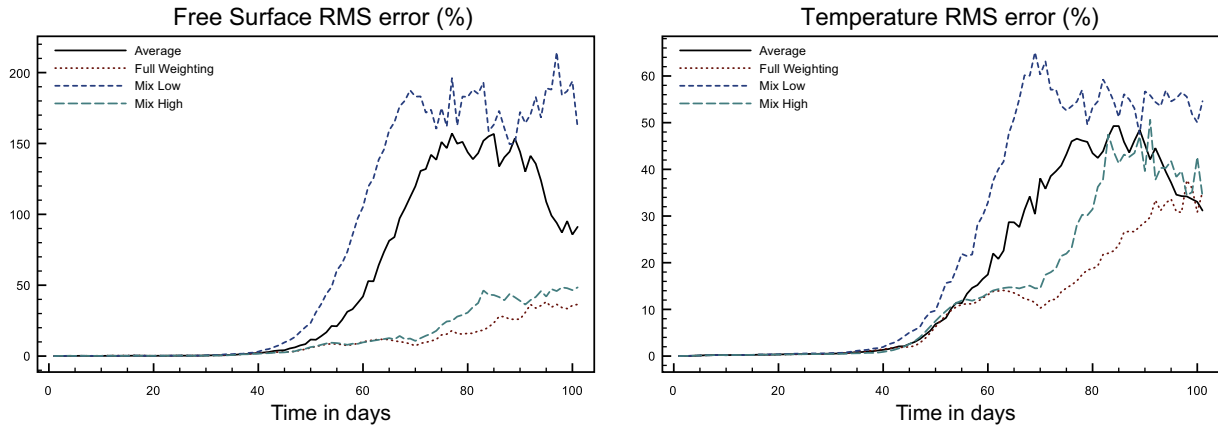


**Fig. 17.** Normalized RMS error [%] in the vortex test case for free surface elevation (left) and temperature (right). In the nesting procedure, interface separation is applied without sponge layer.

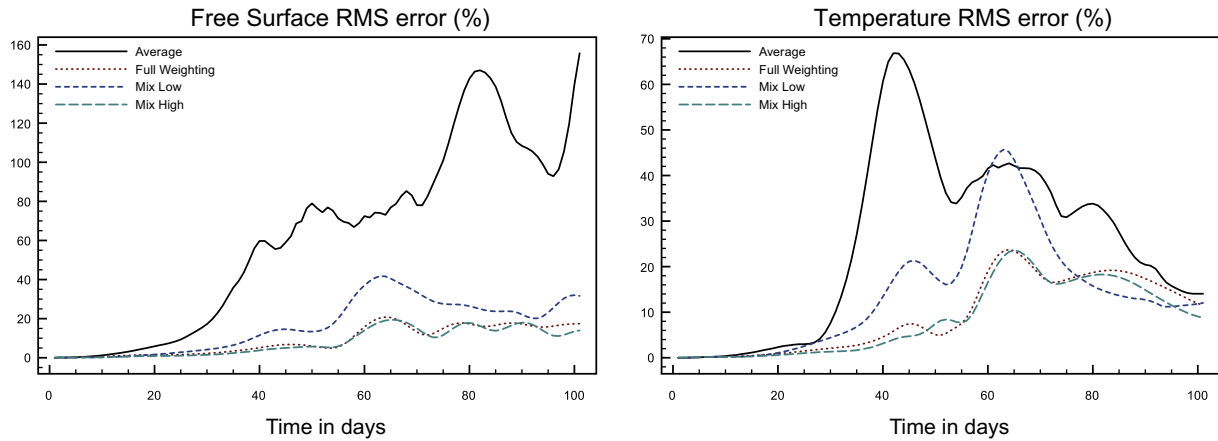


**Fig. 18.** Normalized RMS error [%] in the vortex test case for free surface elevation (left) and temperature (right). In the nesting procedure, a sponge layer is applied but not interface separation.

tions are made without sponge layers and without separated dynamic and feedback interfaces. Fig. 15 shows the solutions obtained using four different update schemes: average, full-weighting, *update\_mix\_low* and *update\_mix\_high*. Note that additional experiments using either a direct-injection update scheme (copy of child values at corresponding locations of the parent grid with no spatial filtering) or the Shapiro update scheme are not shown since they both lead to unstable solutions (the simulation ‘blows up’ at day 3 for direct-injection and at day 7 for Shapiro).

The simulations based on the average and *update\_mix\_low* operators lead to noisy solutions where the coarse solution is contaminated by fine scale structures (Fig. 15). Normalized RMS errors are given in Fig. 16; for comparison, it also includes the results from the one-way simulation presented by Penven et al. (2006). This analysis shows that usual updating procedures can be detrimental to the physical solution and cause a degradation of the one-way procedure (for example, Average update in Fig. 16). However, a more sophisticated update scheme, such as the full-weighting, can yield a 50% improvement over the one-way solution by enhancing continuity at the grids interface. As stated earlier, the average operator is unable to damp the small scale modes approaching the interface, which leads to the degradation of the solution. In the one-way and full-weighting two-way solutions, the largest errors occur as the vortex crosses the interface (around day 50) while using the average operator they occur much earlier, when the first dispersed Rossby waves have reached the interface.

In the absence of additional diffusion, low order restriction operators (average, *update\_mix\_low*) are thus very sensitive to small perturbations.

### 3.3. Sponge layer and separation of dynamical/feedback interfaces

Separation of dynamical and feedback interfaces requires the application of a sponge layer to prevent the drift of the fine solution in the zone between dynamical and feedback interfaces. Interfaces separation alone does not improve and even increases RMS errors (Fig. 17). In this case again, high order restriction operators present lower RMS error than their low order equivalent. A sponge layer alone (using maximum diffusivity  $\mu_0 = 500 \text{ m}^2 \cdot \text{s}^{-1}$  for both tracers and momentum) is not much better at reducing the noise associated with low order restriction operators (Fig. 18). The combination of both methods results in a clear improvement (by about 30%) for all simulations (Fig. 19). The normalized RMS error on free surface does not exceed 12% (compared to 40% in one-way simulations). This improvement results from the suppression of the feedback of the largest errors from the fine solution (generally located at the closest point from the interface) into the coarse solution. The fact that the solution is now much less sensitive to the choice of restriction operator is the result of (1) not updating errors created near the interface and (2) damping small scales by the sponge layer, thus in effect replacing the inner-filtering of high order restriction operators. Therefore, weaknesses of low order restric-

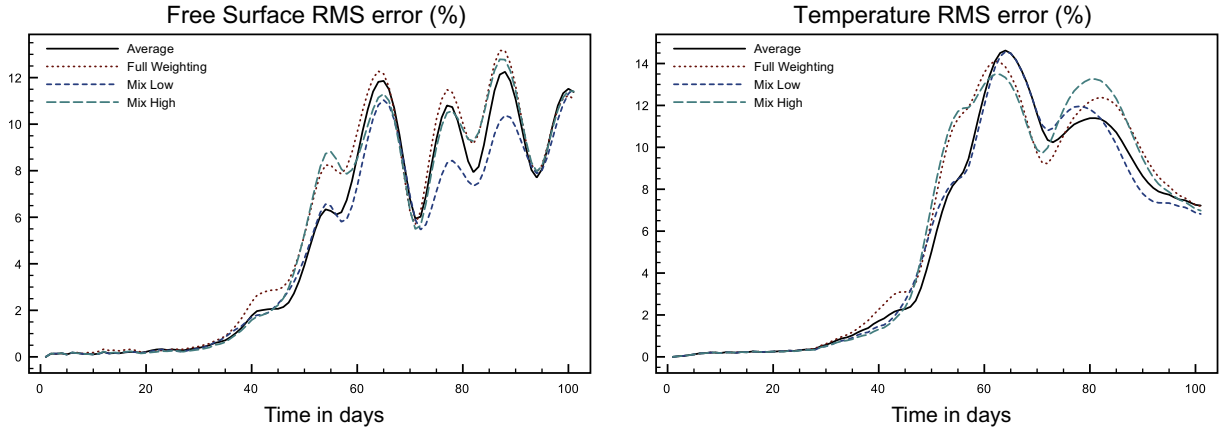


**Fig. 19.** Normalized RMS error [%] in the vortex test case for free surface elevation [m] (left) and temperature (right). In the nesting procedure, both sponge layer and interface separation are applied.

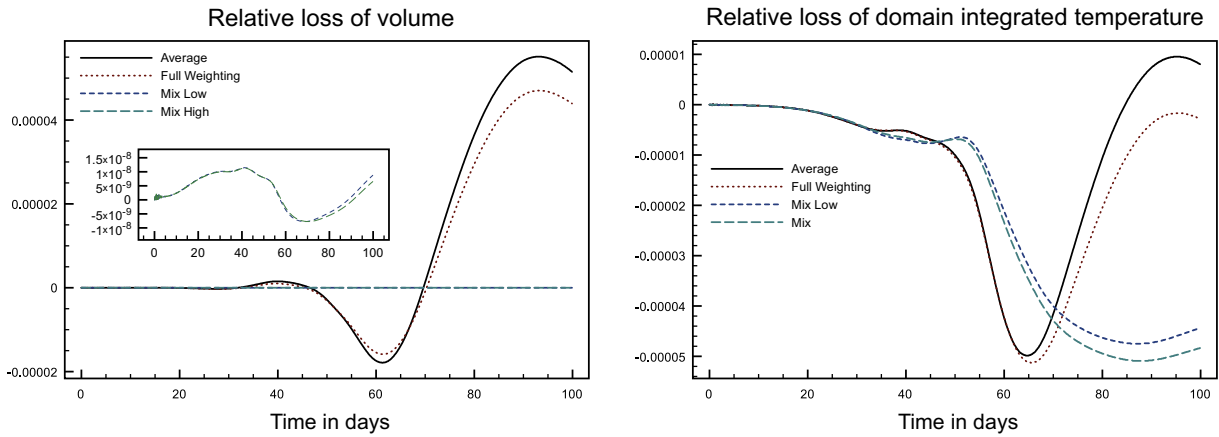


**Fig. 20.** Time evolution of relative loss of volume (left) and temperature (right) resulting from not enforcing conservation in the two-way coupling. The subview inside the left panel shows the small residual volume loss of Mix Low and Mix High schemes.

tion operators can be partially overcome by additional techniques. Yet, they remain sensitive to the choice of these techniques, in particular to diffusivity values as illustrated in the sponge-free case (Fig. 17), and we expect that they perform differently on various model applications. The robustness of high order operators will indeed be fully revealed in the realistic experiments of Section 4.

### 3.4. Conservation

We now analyze the effects of maintaining conservation using the refluxing algorithm described in Section 2.4. As a first step, the computation of the fluxes misfit between high and coarse resolution, as given by Eq. (13), are implemented as a diagnostic tool. Fig. 20 shows the results of accumulated fluxes misfit for volume (free surface) and temperature. Plotted quantities correspond to

$$\delta\eta = \frac{Q_\eta^n - Q_\eta^0}{Q_\eta^0}, \quad Q_\eta^n = \int_S (H_0 + \eta^n) dx,$$

$$\delta T = \frac{Q_T^n - Q_T^0}{Q_T^0}, \quad Q_T^n = \int_\Omega T^n dx$$

where the discrete expressions of  $Q_\eta^n$  and  $Q_T^n$  are computed according to Eq. (15). Note that the subscripts in Q now design the variables  $\eta$  and  $T$ , and Q is integrated over the domain  $\Omega$ . As explained in paragraph Section 2.4.2, *update\_mix\_low* and *update\_mix\_high* operators are intrinsically more conservative. In particular,

they lead to a nearly exact conservation of volume. However, they cannot prevent a heat loss.

Heat and mass loss can be exactly corrected by the refluxing procedure. To assess whether this correction affects the other properties of the nesting schemes, the normalized RMS errors for both free surface and temperature are presented in Fig. 21 (where the solutions with and without conservation are compared). Note that this is done only for the *update\_mix\_low* and *update\_mix\_high* operators since the other restriction operators do not preserve constancy when the refluxing procedure is applied. In addition, the sponge layer diffusion coefficient  $\mu_0$  was increased to a high value of  $1000 \text{ m}^2 \cdot \text{s}^{-1}$  in order to maintain stability in the simulations. This is in agreement with the analysis of paragraph Section 2.4.4, which predicts instability for the second-order mid-point interpolation used in ROMS advection scheme (that globally produces a third order accurate scheme in a finite difference sense). Other experiments (not shown here) confirm that this increase of viscosity does not affect the conclusion of our sensitivity study on conservation. This analysis shows that enforcement of conservation leads to a small increase in RMS error, which is not in contradiction with the analysis of Section 2.4.4.

### 3.5. Coarse grid improvement

Finally, we analyze the vortex solution in the parent domain (outside the refinement area) starting from the time when it begins

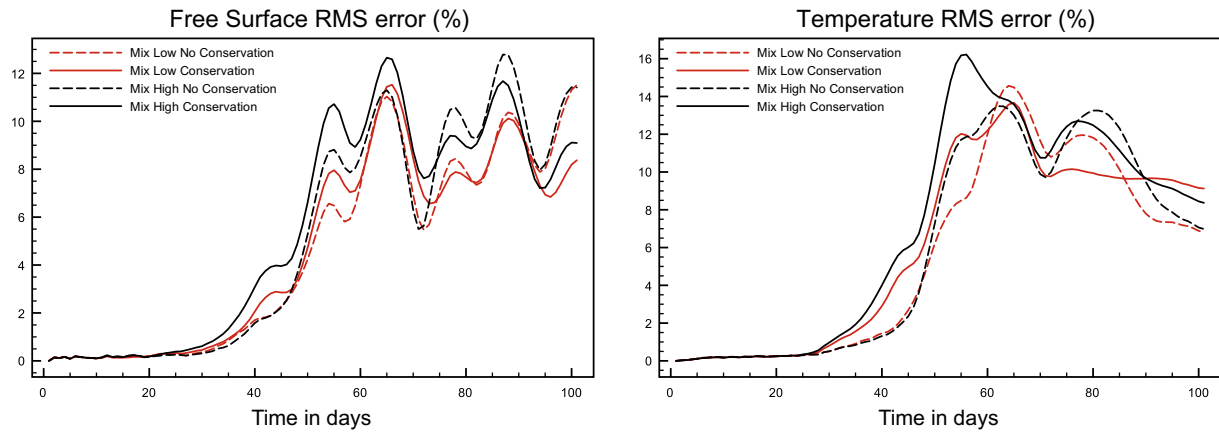


Fig. 21. Normalized RMS error [%] for free surface and temperature with and without conservation.

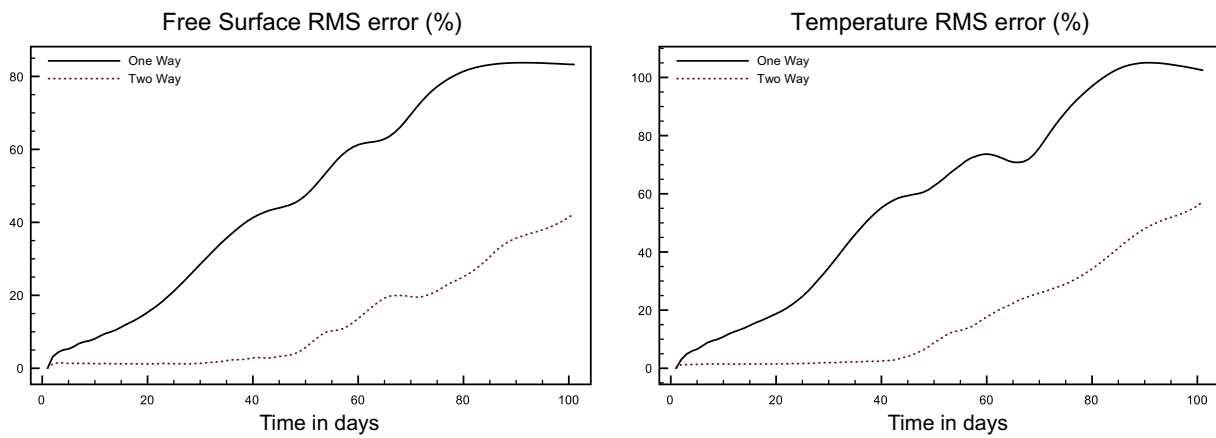


Fig. 22. Normalized RMS error [%] on the coarse grid domain for free surface (left) and temperature (right) and for the one-way solution (the error is in this case the same as in the uniformly coarse resolution case) and two-way solution.

to cross the interface. Normalized RMS errors are indicated in Fig. 22. When the vortex is located inside the refinement area, the coarse solution error in two-way nesting is close to the fine solution error which is very small. In one-way nesting, degradation due to the dominance of wave dispersion over advective axisymmetrization effects is rapidly apparent as the coarse solution gets no feedback from the fine grid (Fig. 12). As the vortex crosses the interface (around day 50), the two-way solution starts to degrade as well. However, the error remains much smaller than in the one-way experiment. This experiment illustrates the lasting benefit of two-way coupling beyond the refinement area, a capability that is of particular interest in the context of upscaling and teleconnection processes.

#### 4. Two-way nesting for the California Current System

The two-way nesting algorithm selected from the previous analysis is now tested in a realistic configuration that covers the full spectrum of dynamical scales and large topographic variations (this is the same procedure as presented by Penven et al. (2006) for the one-way algorithm).

The reference experiment (REF) is an equilibrium solution of the California Current System (CCS) at 5 km resolution (Marchesiello et al., 2003). It is compared with an equivalent simulation at 15 km resolution (LOW) and 2 experiments based on a 5 km coastal grid nested in this larger scale model. A first simulation is made

using only one-way nesting (1-WAY), the other is based on the two-way methodology described above (2-WAY). Because ROMS numerical schemes have evolved since its first applications in the CCS (essentially the pressure gradient algorithm, equation of state, barotropic time stepping and barotropic/baroclinic coupling algorithm; see Shchepetkin and McWilliams, 2009, for a review), these new solutions are similar but not identical to the results obtained previously (Marchesiello et al., 2003; Penven et al., 2006). There are also several differences in the configuration parameters. First, the topography (based on GEBCO, <http://www.gebco.net/>) is regridded to ensure volume equality between the nested grid and REF. Second, the western boundary of the nested grid is pushed 100 km further offshore to encompass the main coastal transition zone. Third, initial and large scale boundary conditions are derived, using ROMSTOOLS (Penven et al., 2008), from the World Ocean Atlas 2005 (Conkright et al., 2002). Note that, as described by Penven et al. (2006), a smooth transition between coarse and fine gridded topography is provided within 5 coarse-grid points of the interface (the topographies on the first two grid points are identical).

Algorithmic choices for two-way nesting in the CCS simulations were made on the basis of both theoretical arguments and results of the ideal test case presented earlier. These choices are: (1) nesting at the barotropic level; (2) either “low” (*Mix Low*) or “high” (*Mix High*) order update schemes; (3) dynamical and feedback interfaces separation (4) sponge layer acting on the difference between fine and coarse solutions (with maximum diffusivity  $\mu_0 = 250 \text{ m}^2 \cdot \text{s}^{-1}$  for tracers and  $\mu_0 = 125 \text{ m}^2 \cdot \text{s}^{-1}$  for momentum).

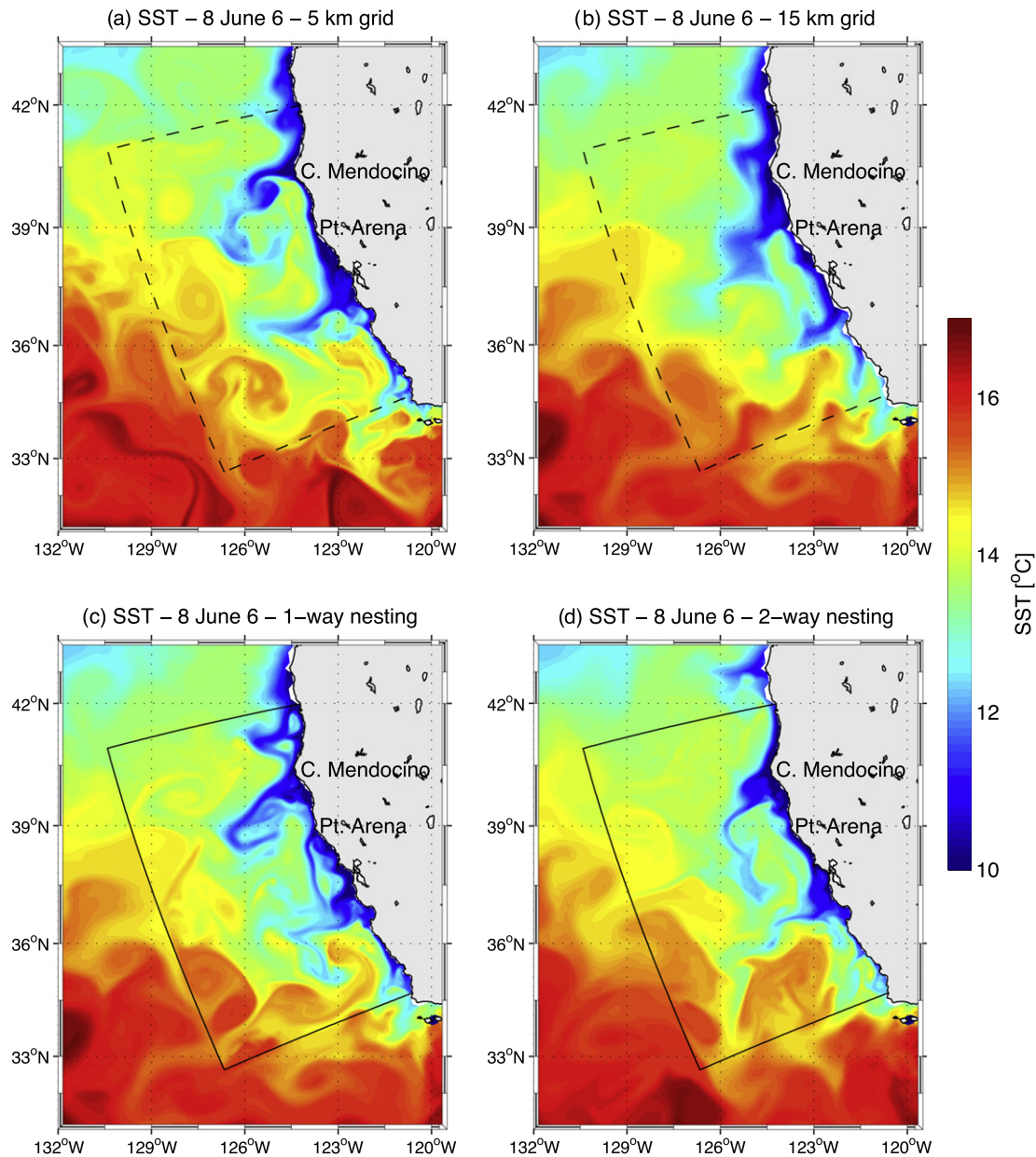


**Fig. 23.** Sea surface temperature [°C] for 8 June of model year 6. a: REF. b: LOW. c: 1-WAY. d: 2-WAY.

Volume conservation is also constrained. However, tracer flux correction was not fully satisfying, with stability problems arising in the course of the long-term simulation. We believe this to be a result of two main problems. In Subsections 2.4.4 and 3.4, we noted a potential instability associated with the flux correction algorithm when even order midpoint-interpolation are used, as is the case in ROMS. But maybe more importantly, the connection area for realistic simulations with complex topography needs particular attention, especially when flux correction is applied. The latter requires additional constraints on the discrete form of the topography along the interface.<sup>2</sup> Nevertheless, the absence of tracer

conservation enforcement in the following experiments did not lead to any significant drift of the solutions.

All experiments are integrated for 10 years. Analyses are performed from years 4 to 10. Fig. 23 represents sea surface temperature (SST) on June 8 of year 6 (same dates as in Penven et al., 2006) for the 4 experiments. Typical summer SST patterns in REF (Fig. 23(a)) represent upwelled coastal waters, upwelling fronts and filaments extending from the major capes. These intra-seasonal features are of chaotic nature (Marchesiello et al., 2003), i.e., they cannot be compared individually at any particular time but only in a statistical way. We will thus focus on patterns and their potential alteration by the nested interface. Next, mean and variance fields will be analysed, keeping in mind that 7 years of sampling is too short to properly reduce the standard error of estimators. Only large regional features will thus be compared as opposed to small-scale details.

In LOW (Fig. 23(b)), the fronts are more diffuse and the overall pattern is smoother. Coastal upwelling is also less intense. As de-

<sup>2</sup> We are currently investing this issue. One possible solution could be an extension of an algorithm proposed by Haley and Lermusiaux (2010, see their Appendix C.1.1): topography smoothing, constrained by the slope parameter for reducing pressure gradient errors, must be also made consistent with restriction operators in the connection area and, in our case, with the flux correction procedure.

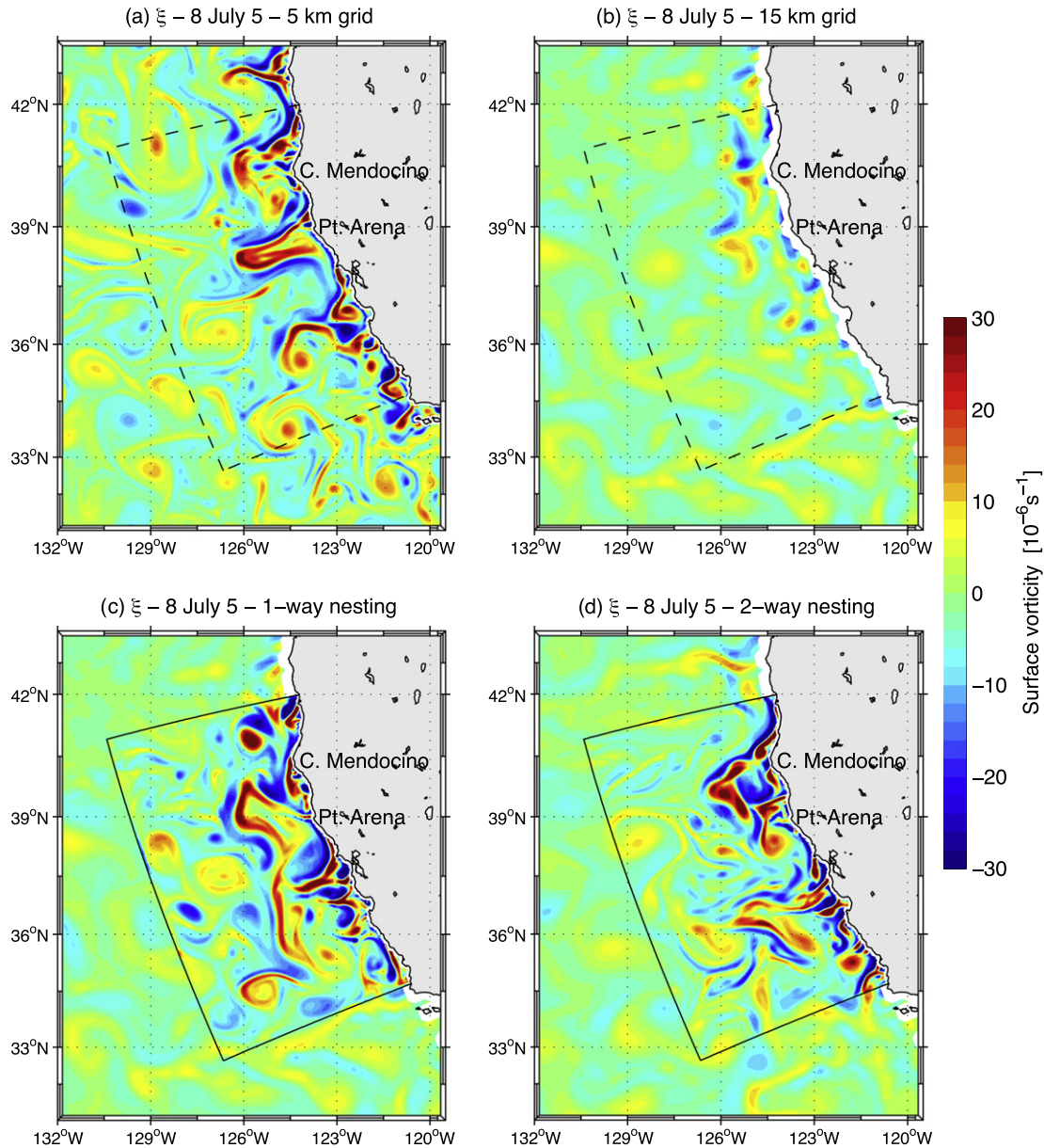


Fig. 24. Sea surface vorticity [ $10^6 \text{ s}^{-1}$ ] for 8 July of model year 5. a: REF. b: LOW. c: 1-WAY. d: 2-WAY.

scribed by Penven et al. (2006), 1-WAY is able to recover the general SST patterns observed in REF: upwelling fronts and filaments (Fig. 23(c)). However, discontinuities are apparent at the parent-child interface, while they never occur in the simulation with two-way nesting (Fig. 23(d)).

Surface vorticity can be used as an indicator of flow discontinuities at the interface. It is displayed in Fig. 24 for July 8 of year 5. In REF (Fig. 24(a)), we recognize the strong negative/positive values associated with coastal jets, upwelling filaments streaming offshore, and a collection of offshore cyclonic and anticyclonic eddies. These structures almost disappear in LOW (Fig. 24(b)). In 1-WAY, there is no major discernible discontinuity at the boundaries (Fig. 24(c)), but there are meaningful differences with REF: eddies tend to concentrate near the western interface, probably affecting the offshore extension and propagation of coastal features. This accumulation of eddy energy seems absent in 2-WAY (Fig. 24(d)); note the offshore eddy at [128°W, 38°N] which evolves around the interface), resulting in turbulent patterns resembling those of REF.

The mean sea surface height (SSH) in REF (Fig. 25(a)) exhibits the 3 large meanders of the CCS described by Marchesiello et al. (2003). In this new simulation, they appear slightly less prominent but they are similarly located: off Cape Mendocino, Monterey Bay and Point Conception. They are also present in LOW (Fig. 25(b)) but the detachment of the flow at Cape Mendocino is delayed, resulting in a southward shift of the general pattern. In 1-WAY and 2-WAY (Fig. 25(c) and (d)), the detachment at Cape Mendocino is similar to REF, as well as the re-attachment of the flow along the coast off Point Arena, and the detachment north of Monterey Bay. 1-WAY amplifies the meanders near the southern boundary of the child domain and underestimates the northern meander. Overall, 2-WAY is a closer solution to REF, albeit with some discrepancies (stronger currents near the northern child boundary). This suggests that the northern interface between coarse and fine grids is situated at a critical point with respect to the dynamics of the CCS, as discussed by Penven et al. (2006).

The following comparisons illustrate the performance of nesting in maintaining the mean statistical characteristics of mesoscale

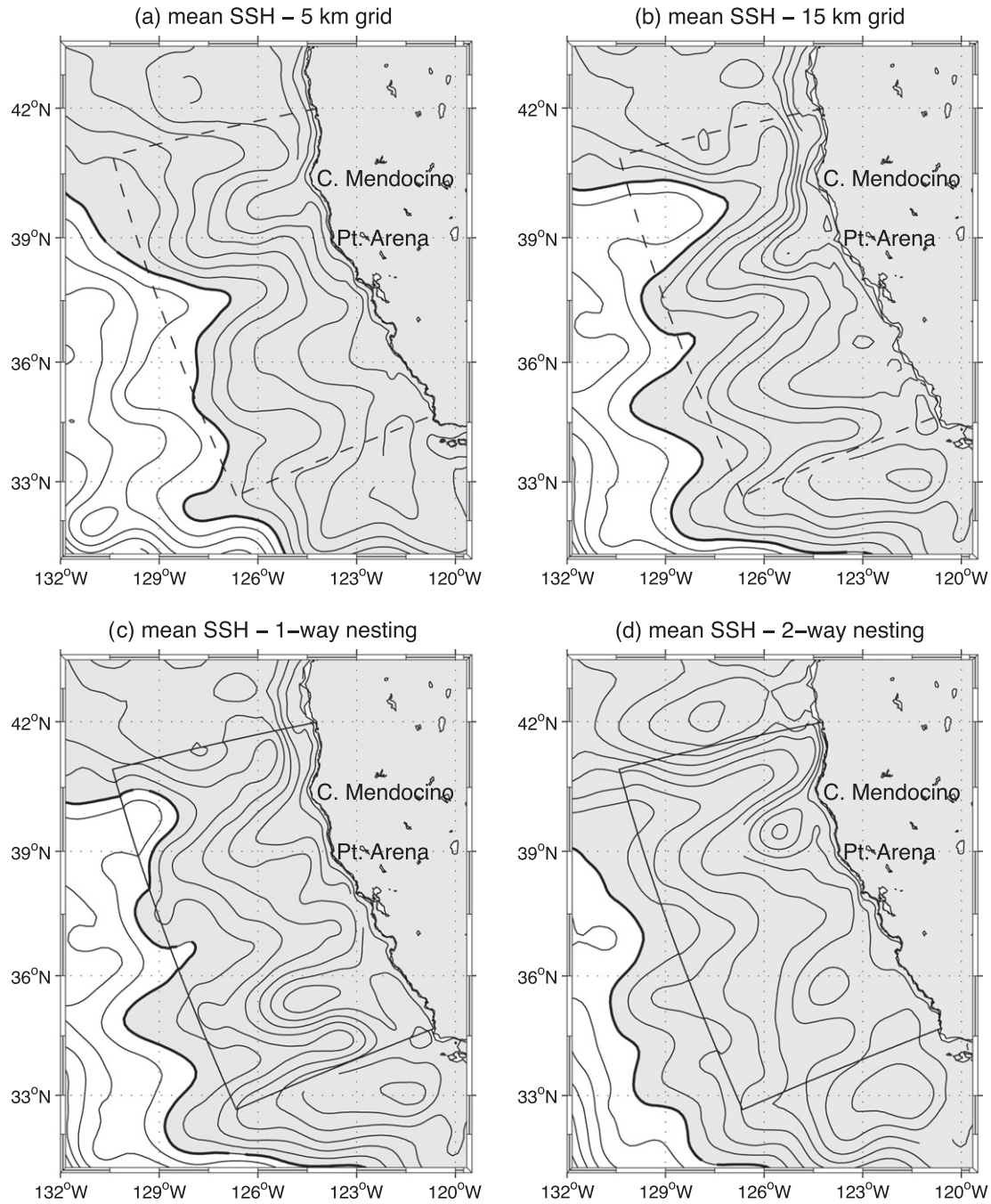


**Fig. 25.** Mean sea surface height (SSH) [cm]. a: REF. b: LOW. c: 1-WAY. d: 2-WAY.

variability. The SSH standard deviation (or root mean square: RMS SSH) is a measure of CCS variability. In REF, maximum values of 6 to 8 cm are produced offshore in the core of the CCS (Fig. 26(a)); a maximum of 8 cm is located off Cape Mendocino. RMS SSH is at least 30% lower in LOW (Fig. 26(b)); 1-WAY and 2-WAY recover most of the patterns observed in REF, but 1-WAY shows excessive variability along the western interface (Fig. 26(c)), which is absent from 2-WAY (Fig. 26(d)). Interestingly, some mesoscale variability is preserved outside the refinement area in the two-way nested solution, which emphasizes the improvement that refinement may provide to connected areas.

A final experiment shows that 2-WAY is sensitive to the update procedure, consistently with the baroclinic vortex test case: using *update\_mix\_low* in place of *update\_mix\_high*, the solution appears

degraded (compare Fig. 27 with Figs. 25 and 26). This is particularly true in the southern part of the child domain, around 35°N, where excessive variability is generated close to the boundary by *update\_mix\_low* in comparison with the reference solution and the solution produced by *update\_mix\_high* (Fig. 27b and Fig. 26). This result again illustrates the inability of low order update schemes to filter unresolved scales, and the limited usefulness of sponge layers.

These experiments provide a demonstration that the selected two-way nested algorithm is stable and accurate for long-term integrations of regional oceanic configurations. It also confirms that two-way is an improvement to one-way nesting in various ways: continuity of fine and coarse solutions at the grids interface; dynamical integrity of the solutions in the refinement area (as a re-

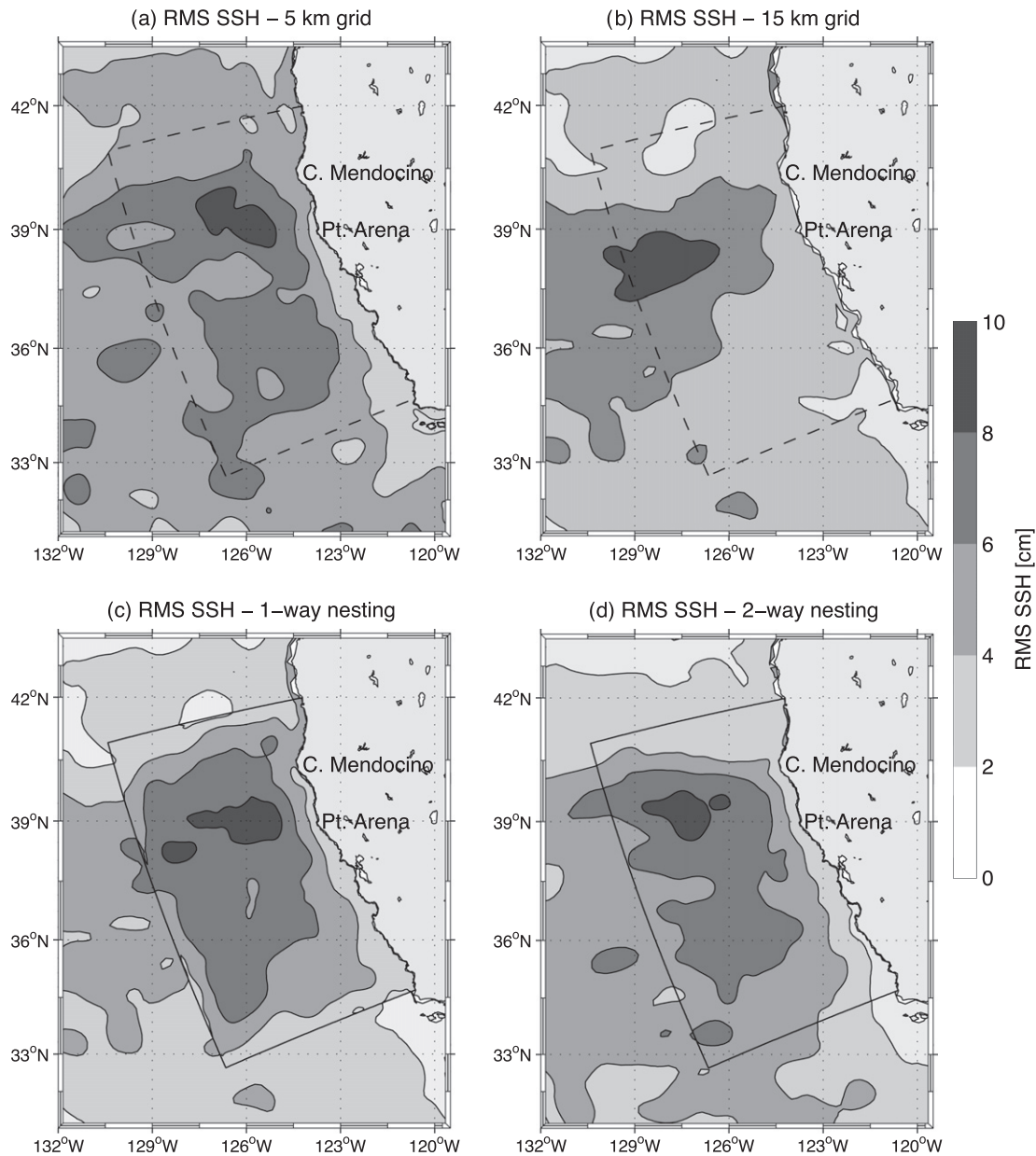


Fig. 26. Root mean square of sea surface height (RMS SSH) [cm]. a: REF. b: LOW. c: 1-WAY. d: 2-WAY.

sult of better interface transparency); and improvements outside the refinement area.

## 5. Conclusion

Algorithms for the implementation of two-way interactions in a split-explicit free surface ocean model were described. A new solution was proposed for the coupling between coarse and fine grid solutions at the barotropic level based on the introduction of intermediate averaged values. Solutions to the conservation problem using a flux correction algorithm was proposed and its stability was analyzed. The key role of the update scheme is also emphasized and the use of a full-weighting operator is proposed for its excellent properties regarding the filtering of small scale features.

These developments were implemented in ROMS and tested in the idealized framework of a baroclinic vortex. A comparison with a reference solution computed at high resolution shows agreement

in the refinement area and improvements in the coarse grid area as well. Normalized RMS errors do not exceed 12% for free surface elevation and 14% for temperature after 100 days of integration. They are small in comparison with one-way simulations and previous two-way implementations tested with the same idealized case.

The selected nesting algorithm is part of ROMS\_AGRIF (a nested version of ROMS) and is freely available under CeCILL-C license at the ROMS\_AGRIF website (<http://roms.mpl.ird.fr/>). It is fully compatible with ROMS parallel capabilities on both shared and distributed memory architectures (OPEN\_MP or Message Passive Interface protocols). It has been successfully tested in a realistic simulation of the California Current System and clearly improves over one-way nested algorithms on interface continuity and dynamical integrity of the fine and coarse solutions. The nesting implementation of ROMS\_AGRIF allows several levels of embedding and several grids at one particular level. These capabilities, combined with the inner qualities of our two-way nesting algo-

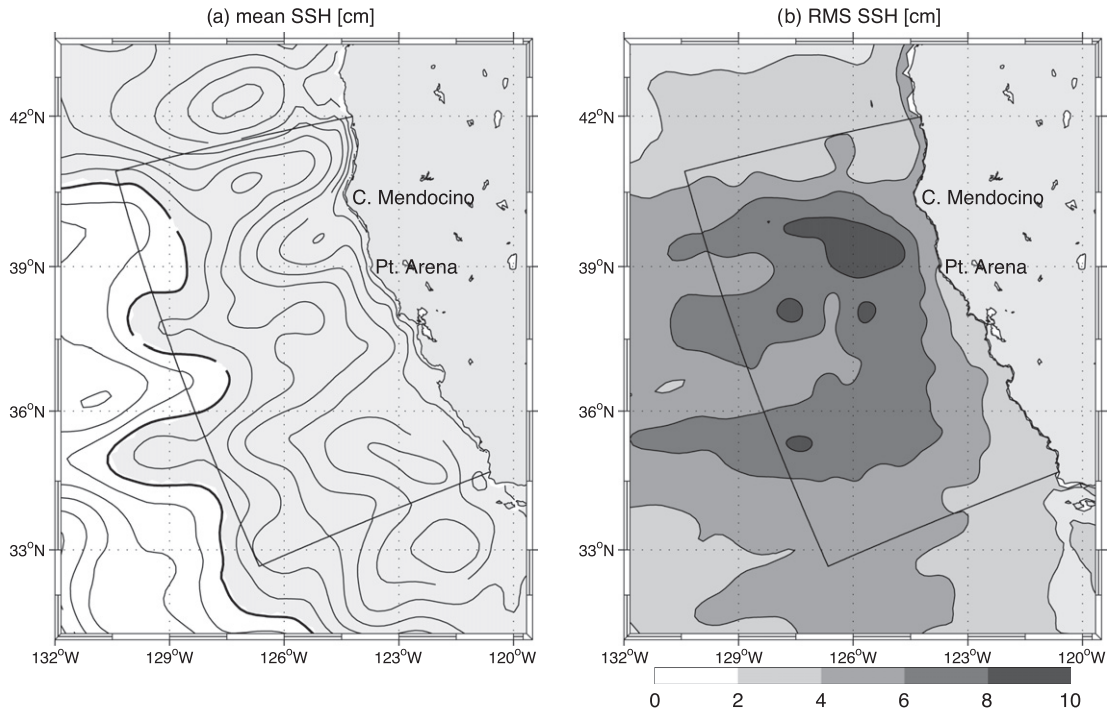


Fig. 27. Mean and RMS SSH [cm] in the 2-WAY experiment with *update\_mix\_low*.

rithm and generally high-order accuracy of ROMS numerics, allow for realistic simulations of coastal and ocean dynamics at multiple scales, and of upscaling and teleconnection problems.

### Appendix A. Weights computation

To obtain intermediate averaged values, there are several ways to compute weights satisfying (7). Here, a simple method is described. Weights for  $\alpha = M^*$  are fixed by the second condition in (7). The other weights are defined by a recurrence formula backward in time. If we suppose that  $a_{m,\alpha}$  are normalized and centered at time  $t = t^n + \frac{\alpha}{M^*} \Delta t$  then we search for weights  $a_{m,\alpha-1}$  normalized and centered at time  $t = t^n + \frac{(\alpha-1)}{M^*} \Delta t$  with a simple combination:

$$a_{m,\alpha-1} = \mu a_{m,\alpha} + \nu a_{m+1,\alpha} \quad (\text{A.1})$$

It can be shown that normalization and centering respectively imply the two following relations to be satisfied by  $\mu$  and  $\nu$

$$\mu (1 - a_{\alpha,\alpha}) + \nu (1 - a_{0,\alpha}) = 1 \quad (\text{A.2})$$

$$\mu \left( \frac{\alpha}{M^*} M - a_{\alpha,\alpha} \alpha \right) + \nu \left( \frac{\alpha}{M^*} M - 1 + a_{0,\alpha} \right) = \frac{\alpha-1}{M^*} M \quad (\text{A.3})$$

Eqs. (A.2) and (A.3) are solved for  $(\mu, \nu)$ . The discriminant of the system is given by

$$\Delta = \frac{\alpha}{M^*} M (a_{0,\alpha} - a_{\alpha,\alpha}) + [1 - a_{0,\alpha}] [(\alpha+1) a_{\alpha,\alpha} - 1]$$

There is one particular case for which the discriminant vanishes: the case of flat weights over  $[1:M^*]$  for which  $M^* = 2M$ ,  $a_{m,M^*} = \frac{1}{M^*+1}$ ,  $\forall m$ . The discriminant vanishes but the system is compatible since both Eqs. (A.2), (A.3) can be rewritten as

$$\mu + \nu = \frac{M^* + 1}{M^*}$$

From (A.1)  $a_{m,M^*-1} = \frac{1}{M^*}$  and by recurrence

$$a_{m,\alpha} = \frac{1}{\alpha+1}, \quad \forall \alpha, \forall m$$

The intermediate coefficients are simply rescaled from the original ones. In more general cases, it seems difficult to find conditions on  $a_m$  so that the discriminant never vanishes. For all typical tested filters, it does not.

### References

- Barth, A., Alvera-Azcárate, A., Rixen, M., Beckers, J.-M., 2005. Two-way nested model of mesoscale circulation features in the ligurian sea. *Prog. Oceanogr.* 66, 171–189.
- Berger, M.J., Colella, P., 1989. Local adaptive mesh refinement for shock hydrodynamics. *J. Comput. Phys.* 82, 64–84.
- Berger, M.J., Olinger, J., 1984. Adaptive mesh refinement for hyperbolic partial differential equation. *J. Comput. Phys.* 53, 484–512.
- Biastoch, A., Böning, C.W., Lutjeharms, J.R.E., 2008. Agulhas leakage dynamics affects decadal variability in atlantic overturning circulation. *Nature* 456, 489–492.
- Blumberg, A.F., Mellor, G.L., 1987. A description of a three-dimensional coastal ocean circulation model. In: Heaps, N. (Ed.), *Three-Dimensional Coastal Ocean Models*, vol. 4. American Geophysical Union, p. 208.
- Bryan, F., 1969. A numerical method for the study of the circulation of the world ocean. *J. Comput. Phys.* 4, 347–376.
- Conkright, M.E., Locarnini, R.A., Garcia, H.E., O'Brien, T.D., Boyer, T.P., Stephens, C., Antonov, J.I., 2002. *World Ocean Atlas 2001: Objective Analyses, Data Statistics, and Figures*, CD-ROM Documentation. Technical report, National Oceanographic Data Center, Silver Spring, MD.
- Debreu, L., Blayo, E., 2008. Two-way embedding algorithms: a review. *Ocean Dyn.* 58, 415–428.
- Deleersnijder, E., Legat, V., Lermusiaux, P.F.J., 2010. Multiscale modelling of coastal, shelf and global ocean dynamics. *Ocean Dyn.* 60, 1357–1359.
- Dukowicz, J.K., Smith, R.D., 1994. Implicit free-surface method for the Bryan–Cox–Semtner ocean model. *J. Geophys. Res.* 99, 7991–8014.
- Haley, P.J., Lermusiaux, P.F.J., 2010. Multiscale two-way embedding schemes for free-surface primitive-equations in the multidisciplinary simulation, estimation and assimilation system. *Ocean Dyn.* 60, 1497–1537.
- Ham, D.A., Pain, C.C., Hanert, E., Pietrzak, J., Schröter, J., 2009. Special issue: the sixth international workshop on unstructured mesh numerical modelling of coastal, shelf and ocean flows. Imperial College London, september 1921, 2007. *Ocean Model.* 28, 1.
- Hanert, E., Roux, D.Y.L., Legat, V., Deleersnijder, E., 2004. Advection schemes for unstructured grid ocean modelling. *Ocean Model.* 7, 39–58.
- Hemker, P.W., 2001. On the order of prolongations and restrictions in multigrid procedures. *J. Comput. Appl. Math.* 32, 423–429.
- Killworth, P.D., Stainforth, D., Webb, D.J., Paterson, S.M., 1991. The development of a free-surface Bryan–Cox–Semtner ocean model. *J. Phys. Oceanogr.* 21, 1333–1348.

- Laugier, M., Angot, P., Mortier, L., 1996. Nested grid methods for an ocean model: a comparative study. *Int. J. Numer. Methods Fluids* 23, 1163–1195.
- Levin, C., Iskandarani, M., Haidvogel, D., 2006. To continue or discontinue: comparisons of continuous and discontinuous Galerkin formulations in a spectral element ocean model. *Ocean Model.* 15, 56–70.
- Maddison, J.R., Marshall, D.P., Pain, C.C., Piggott, M.D., 2011. Accurate representation of geostrophic and hydrostatic balance in unstructured mesh finite element ocean modelling. *Ocean Model.* 39, 248–261.
- Marchesiello, P., McWilliams, J.C., Shchepetkin, A., 2001. Open boundary condition for long-term integration of regional oceanic models. *Ocean Model.* 3, 1–21.
- Marchesiello, P., McWilliams, J.C., Shchepetkin, A., 2003. Equilibrium structure and dynamics of the California Current System. *J. Phys. Oceanogr.* 33, 753–783.
- Marchesiello, P., Capet, X., Menkes, C., Kennan, S.C., 2011. Submesoscale dynamics in tropical instability waves. *Ocean Model.* 39, 31–46.
- McWilliams, J.C., Flierl, G.R., 1979. On the evolution of isolated nonlinear vortices. *J. Phys. Oceanogr.* 9, 1155–1182.
- Penven, P., Debreu, L., Marchesiello, P., McWilliams, J.C., 2006. Application of the ROMS embedding procedure for the central California upwelling system. *Ocean Model.* 12, 157–187.
- Penven, P., Marchesiello, P., Debreu, L., Lefèvre, J., 2008. Software tools for pre- and post-processing of oceanic regional simulations. *Environ. Model. Soft.* 23, 660–662. <http://dx.doi.org/10.1016/j.envsoft.2007.07.004>.
- Sannino, G., Herrmann, M., Carillo, A., Rupolo, V., Ruggiero, V., Artale, V., Heimbach, P., 2009. An eddy-permitting model of the mediterranean sea with a two-way grid refinement at the strait of gibraltar. *Ocean Model.* 30 (1), 56–72.
- Shchepetkin, A.F., McWilliams, J.C., 2005. The regional oceanic modeling system (ROMS): a split-explicit, free-surface, topography-following-coordinate oceanic model. *Ocean Model.* 9, 347–404.
- Shchepetkin, A.F., McWilliams, J.C., 2009. Correction and commentary for Ocean forecasting in terrain-following coordinates: Formulation and skill assessment of the regional ocean modeling system by Haidvogel et al. *J. Comput. Phys.* 227, 3595–3624.
- Sidorenko, D., Wang, Q., Danilov, S., Schröter, J., 2011. Fesom under coordinated ocean-ice reference experiment forcing. *Ocean Dyn.* 61, 881–890.
- Spall, M.A., Holland, W.R., 1991. A nested primitive equation model for oceanic applications. *J. Phys. Oceanogr.* 21, 205–220.
- Warner, J.C., Geyer, W.R., Arango, H.G., 2010. Using a composite grid approach in a complex coastal domain to estimate estuarine residence time. *Comput. Geosci.* 36, 921–935.